



### 저작자표시-비영리-동일조건변경허락 2.0 대한민국

이용자는 아래의 조건을 따르는 경우에 한하여 자유롭게

- 이 저작물을 복제, 배포, 전송, 전시, 공연 및 방송할 수 있습니다.
- 이차적 저작물을 작성할 수 있습니다.

다음과 같은 조건을 따라야 합니다:



저작자표시. 귀하는 원저작자를 표시하여야 합니다.



비영리. 귀하는 이 저작물을 영리 목적으로 이용할 수 없습니다.



동일조건변경허락. 귀하가 이 저작물을 개작, 변형 또는 가공했을 경우에는, 이 저작물과 동일한 이용허락조건하에서만 배포할 수 있습니다.

- 귀하는, 이 저작물의 재이용이나 배포의 경우, 이 저작물에 적용된 이용허락조건을 명확하게 나타내어야 합니다.
- 저작권자로부터 별도의 허가를 받으면 이러한 조건들은 적용되지 않습니다.

저작권법에 따른 이용자의 권리는 위의 내용에 의하여 영향을 받지 않습니다.

이것은 [이용허락규약\(Legal Code\)](#)을 이해하기 쉽게 요약한 것입니다.

[Disclaimer](#)

공학박사 학위논문

**Enhancing the Utilization of Visible-  
Light by Controlling the Electronic  
and Photonic Band Structures of  
TiO<sub>2</sub>-based Materials**

가시광 이용률 향상을 위한 이산화티탄 기반  
물질의 전자 및 광밴드 구조 제어

2018년 8월

서울대학교 대학원

화학생물공학부

엄 하 니

## Abstract

# **Enhancing the Utilization of Visible-Light by Controlling the Electronic and Photonic Band Structures of TiO<sub>2</sub>-based Materials**

Ha Nee Umh

School of Chemical and Biological Engineering

The Graduate School

Seoul National University

As industrial development is on going everyday, and the associated research is required for the development of new materials to be applied for energy or environmental areas. TiO<sub>2</sub> is main candidates as photocatalyst, photoelectrode materials due to its noticeable photostability, low cost and nontoxicity. However, challenging point is still existed for employing TiO<sub>2</sub> on practical photocatalytic applications. TiO<sub>2</sub> has wide bandgap (3.2 eV for anatase and 3.0 eV for rutile), which can activate under only within ultraviolet light region. This thesis deals with the engineering the energy band structure of TiO<sub>2</sub> for absorbing the visible light region and how materials are applied to environment and energy areas.

Environmental applications of heterogeneous photocatalysis have been considered among the most effective methods for elimination of many hazardous organic pollutants. Interfacial energy band bending of heterogeneous photocatalyst facilitate the charge transfer, leads to high photocatalytic performance. The modulation the Fermi level of metal change

the electric field of photocatalyst without any electron mediator. The amount and rate of whole charge transfer were directly validated to the photocatalytic performance in the acetaldehyde photooxidation reaction.

Photonic nanostructures are currently attracting considerable attentions due to their property, guiding the light. Structural color has an origin in geometric structures, which differ from the most common color generation associated with the use of pigments or dyes. The hierarchical TiO<sub>2</sub> nanobowl arrays were fabricated by a two-step anodization process where the nanobowl structure brought about two different reflection peaks from its flat bottom and inclined plane. The positions of the two reflection peaks as well as their wavelength gap were simply adjusted by changing the diameter of TiO<sub>2</sub> nanobowls that depended on the anodizing potential. The reflected wavelength gradually increased with changing the periodicity of the TiO<sub>2</sub> nanobowl, as expected from Bragg diffraction theory. This method enabled us to create a broad color distribution with a high contrast and brightness without employing complicated color generation. Combined light trapping in photonic structure and hot electron formation of noble metal provide the design strategy for the visible light responsive photoelectrochemical water splitting.

**Keywords:** Titania, Heterogeneous photocatalyst, Visible-light responsive, Fermi level, Electronic bandgap, Charge separation, Acetaldehyde, Porous structure, Structural color, Photonic crystal, Photonic bandgap, Photoelectrochemical water splitting.

**Student Number:** 2014-30292

# Contents

<b>Chapter 1. Introduction .....</b>	<b>1</b>
<b>1.1 Engineering the Energy Bandgap of Photocatalyst at the Interfaces for Enhanced Visible Light Absorption.....</b>	<b>3</b>
<b>1.2 Tuning the 2D photonic crystal nanostructure for guiding of visible light .....</b>	<b>5</b>
<b>1.3. Objectives.....</b>	<b>6</b>
<b>Chapter 2. Engineering the Energy Bandgap of Photocatalyst at the Interfaces for Enhanced Visible Light Absorption .....</b>	<b>7</b>
<b>2.1 Introduction .....</b>	<b>7</b>
<b>2.2 Experimental.....</b>	<b>10</b>
2.2.1 Preparation of catalysts .....	10
2.2.2 Characterizations .....	10
2.2.3 Electrochemical characterizations .....	11
2.2.4 Photoluminescence spectroscopy .....	12
2.2.5 Photocatalytic performance characterization.....	13
<b>2.3 Results and discussion .....</b>	<b>14</b>
2.3.1 Structural characterization .....	14
2.3.2 Electronic state characterization .....	15
2.3.3 Photoluminescence characterization.....	20
2.3.4 Photooxidation reactivity .....	21
<b>Chapter 3. Tuning the photonic crystal nanostructure for</b>	

<b>guiding of visible light .....</b>	<b>44</b>
<b>3.1 Introduction .....</b>	<b>44</b>
<b>3.2 Experimental.....</b>	<b>47</b>
3.2.1 Fabrication of 2D TiO <sub>2</sub> photonic crystals.....	47
3.2.2 Characterization .....	47
3.2.3 Color printing using a 2D TiO <sub>2</sub> photonic crystals .....	48
3.2.4 Photoelectrochemical water splitting .....	48
<b>3.3 Results and discussion .....</b>	<b>50</b>
3.3.1 Charcterization .....	50
3.3.2 Modified Bragg diffraction theory.....	51
3.3.3 Color Printing.....	53
3.3.4 Photoelectrochemical water splitting .....	55
<b>Chapter 4. Summary and Conclusions.....</b>	<b>73</b>
<b>Bibliography .....</b>	<b>75</b>
<b>국 문 초 록.....</b>	<b>82</b>

# List of Tables

Table 2-1. The pH and temperature condition to control the size of Pt(x)/TiO <sub>2</sub>	24
Table 2-2. Concentration of Pt in Pt(x)/TiO <sub>2</sub> analyzed by ICP analysis.....	25
Table 2-3. Surface area of Pt(x)/TiO <sub>2</sub> and Pt(x) based on BET and CO adsorption analysis.....	26
Table 2-4. Kinetic parameters elicited from results of time-resolved PL spectra of 1 μM RhB in the presence of samples with 405 nm excitation. ....	27
Table 2-5. Electron and hole transfer rate models was especially considered in the Pt(x)/TiO <sub>2</sub> system when the excitation wavelength is 405 nm	28
Table 2-6. Rate constants for charge transfer of TiO <sub>2</sub> and Pt(x)/TiO <sub>2</sub> s extracted from fitted results of time-resolved PL spectra.....	30
Table 3-1. Structural parameters and reflection wavelengths of the synthesized TiO <sub>2</sub> nanobowl arrays with different colors .....	58

# List of Figures

Figure 2-1. Pt NP size distributions of Pt(x)/TiO <sub>2</sub> s with each x value of (a) 1, (b) 3, and (c) 5. ....	31
Figure 2-2. TEM images and Cs-TEM images of Pt(1)/TiO <sub>2</sub> , Pt(3)/TiO <sub>2</sub> , and Pt(5)/TiO <sub>2</sub> . FFT patterns were obtained from Cs-TEM images...	32
Figure 2-3. (a) UV-Vis-DRS and (b) XRD analysis of TiO <sub>2</sub> and Pt(x)/TiO <sub>2</sub> as a function of Pt NP size. ....	33
Figure 2-4. XPS spectra of Pt(x)/TiO <sub>2</sub> s. Binding energies of Pt 4f was shifted to red due to strong M-S interaction. ....	34
Figure 2-5. Pt L3 edge XANES spectra of Pt(x)/TiO <sub>2</sub> s in the light on/off condition. The enlarged insets show the whitenline differences (red) and the next oscillation parts (blue). ....	35
Figure 2-6. Mott–Schottky plot of TiO <sub>2</sub> and Pt(x)/TiO <sub>2</sub> s under dark condition	36
Figure 2-7. Schematic energy diagrams of Pt/TiO <sub>2</sub> systems with Pt NP size variation under visible light irradiation condition. ....	37
Figure 2-8. Schematic diagram explain the in the aspects of kinetics. When electron and hole carrier concentration thermodynamically remains constant, electron transfer from TiO <sub>2</sub> CB to Pt ( $-k_{T \rightarrow P}^+$ ) can be considered as hole transfer from TiO <sub>2</sub> VB to Pt ( $k_{T \rightarrow P}^+$ ) according to the mathematic calculation. ....	38
Figure 2-9. Time-resolved photoluminescence spectra (PL) of TiO <sub>2</sub> and Pt(x)/TiO <sub>2</sub> s in the 1 μM RhB solutions in the presence of samples with 405 nm laser excitation, where emission wavelength is 580 nm.....	39
Figure 2-10.(a) Schematic diagram of Pt(x)/TiO <sub>2</sub> s charge transfer path under visible light excitation. Hole transport is caused by semiconductor excitation, and electron transport is directly induced by metal excitation. (b) Schematic energy band diagram	

	of charge transfer path of Pt/TiO <sub>2</sub> results from the time-resolved PL measurement. Electron transfer rate constants are indicated as black and blue arrows, and a hole transfer rate as red arrows .....	40
Figure 2-11.	(a) Schematic charge transfer path under visible light excitation in the (a) RhB, (b) TiO <sub>2</sub> in RhB, and (c) Pt(x)/TiO <sub>2</sub> in RhB .....	41
Figure 2-12.	Acetaldehyde photodegradation of Pt(x)/TiO <sub>2</sub> under (a) visible light irradiation (>400 nm) and (b) and enlarged inset shows the photocatalytic rate under dark condition. ....	42
Figure 2-13.	The acetaldehyde photocatalytic rate and charge separation constants. Acetaldehyde conversion rates are as denoted by gray bar. Red line indicates the hole transfer rate ( $k_{T \rightarrow P}^+$ ) and blue line show the electron transfer rate ( $k_{R \rightarrow P \rightarrow T}$ ). ....	43
Figure 3-1.	A schematic diagram of the fabrication of TiO <sub>2</sub> nanobowl arrays with a structural color. (a) A Ti sheet was prepared as a source of TiO <sub>2</sub> . (b) TiO <sub>2</sub> nanotubes are formed on the Ti sheet through first anodization step. (c) The oxide layer was removed by using a sticky tape and ultrasonication leaving a hexagonal concave pattern on the Ti sheet. (d) TiO <sub>2</sub> nanobowl arrays with a structural color were fabricated by applying anodizing potential for several seconds .....	59
Figure 3-2.	SEM images of TiO <sub>2</sub> nanobowl arrays with different diameters of air cavities that prepared by altering anodizing potential: (a) 30 V, (b) 40 V, (c) 50 V, (d) 60 V, (e) 65 V, and (f) 75 V. Scale bars indicate a length of 100 nm .....	60
Figure 3-3.	Size distribution histograms of TiO <sub>2</sub> nanobowl arrays that prepared by altering anodizing potential: (a) 30 V, (b) 40 V, (c) 50 V, (d) 60 V, (e) 65 V, and (f) 75 V .....	61
Figure 3-4.	Cross-sectional SEM images of TiO <sub>2</sub> nanobowl arrays which were fabricated at anodizing conditions of (a) 30 V, (b) 40 V, (c)	

	50 V, (d) 60 V, (e) 65 V, and (f) 75 V. Scale bars indicate a length of 100 nm.....	62
Figure 3-5.	Reflectance spectra of TiO <sub>2</sub> nanobowl arrays with different diameter air cavities. The trend (dotted) lines approximate the shift of the peaks with increasing diameter of the nanostructures.	63
Figure 3-6.	The reflection path of incident light on the TiO <sub>2</sub> nanobowl structure followed by modified Bragg diffraction theory .....	64
Figure 3-7.	(a) A Mondrian painting known as <i>Composition with Color Planes and Gray Lines</i> . (b) The reproduced image on a centimeter scale. (c–f) SEM images of selected areas, which illustrate different diameters and uniform alignment of the nanobowls. White scale bar indicates a length of 200 nm. ....	65
Figure 3-8.	Adhesion tape peeling test to analyze the mechanical stability of TiO <sub>2</sub> nanobowl arrays: (a) before the attachment of a tape, (b) a tape attached on the TiO <sub>2</sub> nanobowl arrays, and (c) after the detachment of the tape from the TiO <sub>2</sub> nanobowl arrays.....	66
Figure 3-9.	UV-vis absorbance change of (a) TiO <sub>2</sub> nanobowl arrays with a blue color and (b) a N3 dye coated on the P25 under irradiation by direct sunlight, and (c) N3 dye coated on the P25 under irradiation of fluorescent light for 12 h. Insets are images taken during the stability test. ....	67
Figure 3-10.	TiO <sub>2</sub> nanobowl arrays immersed in various solvents; (a) water, (b) 1 M NaCl, (c) 1 M HNO <sub>3</sub> , (d) 1 M NaOH, (e) ethanol, (f) acetone, (g) benzene, and (h) toluene.. ....	68
Figure 3-11.	TiO <sub>2</sub> nanobowl arrays immersed in various solvents; (a) water, (b) 1 M NaCl, (c) 1 M HNO <sub>3</sub> , (d) 1 M NaOH, (e) ethanol, (f) acetone, (g) benzene, and (h) toluene.. ....	69
Figure 3-12.	TiO <sub>2</sub> nanobowl arrays immersed in various solvents; (a) water, (b) 1 M NaCl, (c) 1 M HNO <sub>3</sub> , (d) 1 M NaOH, (e) ethanol, (f) acetone,	

	(g) benzene, and (h) toluene..	70
Figure 3-13.	TiO <sub>2</sub> nanobowl arrays immersed in various solvents; (a) water, (b) 1 M NaCl, (c) 1 M HNO <sub>3</sub> , (d) 1 M NaOH, (e) ethanol, (f) acetone, (g) benzene, and (h) toluene..	71
Figure 3-14.	TiO <sub>2</sub> nanobowl arrays immersed in various solvents; (a) water, (b) 1 M NaCl, (c) 1 M HNO <sub>3</sub> , (d) 1 M NaOH, (e) ethanol, (f) acetone, (g) benzene, and (h) toluene..	72

# Chapter 1. Introduction

As increasing demand for clean and sustainable energy, it is necessary to design and apply materials that are suitable for the purpose. It is crucial to develop the materials for energy harvesting and storage with competitive performances and durability, that allows their practical applications.

Semiconductor photocatalysis has received tremendous attention over the past few decades, as it may provide viable solutions on energy and environmental issue [1]. Since Fujishima and Honda reported the photocatalytic water splitting using  $\text{TiO}_2$  electrode under ultraviolet (UV) light,  $\text{TiO}_2$  is the semiconductor most widely investigated in areas of photovoltaics and photocatalysis [2]. Although  $\text{TiO}_2$  exhibits outstanding properties such as suitable bandgap, environmental-friendly, and resistance against corrosion materials, wide bandgap of  $\text{TiO}_2$  ( $\sim 3$  eV) is limit for practical applications under visible light. Many researches are investigated for visible-light responsible  $\text{TiO}_2$ , which are categorized into two approaches. One is electronic band structure engineering for enlarging optical response region such as metal deposition, ion doping and dye sensitization. The other is to enhance the interaction of light with semiconductor by using the surface resonance, and light scattering [3].

Herein, the strategies proposed that can be applied to energy systems by modulating energy band and photonic band structure. Bandgap manipulation through interfacial charge at the interfaces of heterogeneous photocatalysts, for enhancing the photocatalytic activity [4]. A synergetic effect on the light harvesting enhancement is accomplished by modulation of electronic and photonic band structure of  $\text{TiO}_2$ . This thesis will be providing an insight that engineering the electronic and photonic bandgap of  $\text{TiO}_2$  and enables the design the energy harvesting system.

## **1.1 Engineering the Energy Bandgap of Photocatalyst at the Interfaces for Enhanced Visible Light Absorption**

Removal of volatile organic components (VOCs) in indoor environment have been attracted attention because undesirable chemical contaminants can severely affect health and environment.  $\text{TiO}_2$  is a widely used semiconductor and studied in photocatalytic approach when Fujishima and Honda reported the photoelectrochemical water splitting using a  $\text{TiO}_2$  in 1972 [2].  $\text{TiO}_2$  based photocatalyst has been investigated to degrade organic pollutants in water due to high photo-activity, low cost, low toxicity and good chemical and thermal stability and air.

However,  $\text{TiO}_2$  have wide bandgap ( $\geq 3$  eV), which limit for practical applications in indoor environments. The controlling of energy band of photocatalyst is required for extending light absorption region. Several strategies have been developed for designing photocatalysts with high efficiency, visible-light-absorbing property in recent years through bandgap engineering such as doping and facet control [5-7]. Considering the bandgap modulation have become the main focus of photocatalytic research for efficient harvesting of solar energy in this research.

In the chapter 2, modulation of electronic band structure of metal was

investigated by controlling the Fermi level of metal at heterojunctioned metal-semiconductor interfaces.  $\text{TiO}_2$  is a good candidate as a support, and Pt was selected on metal cocatalyst. Under visible-light irradiation, Pt/ $\text{TiO}_2$  composite exhibited much higher photocatalytic activity than rutile  $\text{TiO}_2$ , which used for photodegradation of gaseous acetaldehyde. This finding confirm that the modulation of energy band structures effects on the interfaces of heterogeneous photocatalysts and provide a scientific basis for rational design of photocatalyst.

## **1.2 Tuning the 2D photonic crystal nanostructure for guiding of visible light**

Photonic nanostructures that can be found in the natural world produce structural colors and have been widely used as an effective platform for manipulating light propagation [8,9]. The way to produce unique coloration through photonic crystals (PhCs) have been received a lot of interest due to potential platform for enhancing the visible light harvesting. PhCs with different stop-band energies have been generated by several approaches [10,11]. However, these methods involve some factors that need to be overcome, such as sacrificial templates, complicated fabrication process [12], and difficulties associated with large scale production and integration for producing reported-PhCs in spite of a high resolution. Recently, metal plate anodization technique has been reported as a simple and scalable route to the preparation of high-quality arrays of nanostructures [13,14]. Without employing any complex architectures, 2D PhCs enabled a broad color distribution to be created by altering the diameter of the cavities. Such a color printing technique has great promise for practical applications in chapter 3.

### 1.3. Objectives

The objectives of this thesis are designing TiO<sub>2</sub> photocatalysts for environmental and energy application, modifying electronic band and photonic band structures. aspects.

In following section, Chapter 2 report the the rational design of metal-TiO<sub>2</sub> heterogeneous photocatalysts to enhance the charge separation rate for the target photocatalytic oxidation reactions. Control of photocatalytic activity is interpreted by tuning the electronic state at the metal-semiconductor interfaces. Kinetic and mathematical study are included to reveal the effect of charge transfer on photooxidation reactivity.

Chaper 3 discusses the structural control of TiO<sub>2</sub> and investigate the effect on water splitting. The 2D photonic crystal is reported on a highly reproducible and simple method for periodically arranging bowl-like nanostructures of TiO<sub>2</sub> on a thin Ti sheet. 2D periodic nanostructure based on semiconductor substrate provides potential for utilization of visible light.

# **Chapter 2. Engineering the Energy Bandgap of Photocatalyst at the Interfaces for Enhanced Visible Light Absorption**

## **2.1 Introduction**

Understanding of charge separation phenomena occurred at the interface in metal-semiconductor (M-S) heterogeneous photocatalysts is an important point to enhance the photocatalytic reactivity [16-19]. When the light irradiated to M-S interfaces, charge carrier in metal should move to positive or negative direction according to target photocatalytic oxidation or reduction reactions. Electron transfer path and mechanisms using negative charge state on metal have been studied for photoreduction reactions where semiconductor are operated as electron-hole formation [20-22]. Likewise negative charge transfer, positive charge state of metal is also considered for photocatalytic oxidation reaction because positively carrier transfer paths from metal to semiconductor are lacked in photocatalytic oxidation [23,24].

In this chapter, engineering the energy bandgap at the M-S interfaces is studied by controlling the positive charge state of metal nanoparticles supported on titania system. Platinum was selected as a representative co-catalyst. We propose the two effect on charge separation at the M-S interface that can be considered by introducing a positive charge state of metal as

follows: i) The high Schottky barrier are formed by lower Fermi level when the semiconductor is excited by visible light. Transfer of weakly excited electrons can be blocked from semiconductor conduction band (CB) to metal, while the hole carrier from semiconductor valence band (VB) move to metal due to their high electric field. ii) In the metal part, excited positive charge carrier move to semiconductor CB because of interband transition. Interband transition could be considered for an induction of positive charge state on general metal elements [25-28], which occurs in group IB metal elements is different from hot electron formation by local surface plasmon resonance (LSPR) [29,30]. In this study, charge separation mechanism and photocatalytic activity of Pt/TiO<sub>2</sub> material was discussed under visible light irradiation. In this M-S photocatalytic system, excited electrons which have excess energies around 0.1 eV at the semiconductor CB is blocked by Schottky barrier. Pt/TiO<sub>2</sub> show the high Schottky barrier more than 1 eV, resulting difference between the Fermi level of Pt (~5.6 eV) and rutile TiO<sub>2</sub> (~4.1 eV). Therefore, only hole transfer route is possible from semiconductor VB to metal when visible light ( $\lambda > 400$  nm,  $< 3.1$  eV) is irradiated to Pt/rutile TiO<sub>2</sub>. On the other hand, negative charge carrier formed on metal by interband transition overcome the Schottky barrier at the M-S interfaces. Electron from metal move to CB of semiconductor without any electron mediators[31]. Therefore, charge separation is determined resulting from synergetic effect that excited electron transfer from metal to semiconductor CB and hole transfer from semiconductor VB to metal in the Pt/TiO<sub>2</sub> photocatalytic system under visible light. Gaseous acetaldehyde

photooxidation reaction was conducted to verify the correlation between practical photooxidation activities and positive charge extents on Pt. It was verified that the photocatalyst containing more positively charged metal show the significantly increased oxidation reaction rate by synergetic charge separation effect.

## **2.2 Experimental**

### **2.2.1 Preparation of catalysts**

Commercialized rutile TiO<sub>2</sub> (MT-500) was purchased from TAYCA, and chloroplatinic acid (H<sub>2</sub>PtCl<sub>6</sub>·6H<sub>2</sub>O ≥ 99.9%, Sigma-Aldrich) was used as a Pt metal precursor. All precursors were used without further purification. Pt/TiO<sub>2</sub> was synthesized by chemical reduction method adjusting pH and reaction temperature. 0.5 g of TiO<sub>2</sub> and Pt precursor solutions were dispersed in a 150 mL deionized water after prepared sample were treated with sonication for 30 m. 0.02 M NaBH<sub>4</sub> act as a reducing agent. Reducing solution dropwise to the aqueous Pt/TiO<sub>2</sub> dispersed solution, resulting the deposition of 1 wt% Pt nanoparticles(NPs) on TiO<sub>2</sub> surface after stirring for 3 h. As-synthesized samples were separated to gray powders by ultracentrifugation and dried at 60 °C for 12 h.

### **2.2.2 Characterizations**

The samples were reduced in H<sub>2</sub>/Ar atmosphere at 300 °C for 3 h before characterizations. The morphology, size, and lattice of the synthesized Pt/TiO<sub>2</sub> were obtained by transmission electron microscopy (TEM, JEM-2100, JEOL, 200 kV) and Cs corrected TEM with cold field emission gun (Cs-TEM, JEM-ARM200F, JEOL, 200 kV). 150 particles of Pt/TiO<sub>2</sub> were counted to estimate the average size through size distribution histograms.

Ultraviolet-visible diffuse reflectance (UV-Vis DRS) spectra were recorded with a Jasco V670 spectrometer. The measurement ranges from 300 nm to 800 nm. Crystallinity of Pt/TiO<sub>2</sub> were analyzed by using a Rigaku d-MAX2500-PC powder X-ray diffractometer (XRD) operating at 50 kV and 100 mA using CuK $\alpha$  radiation (1.5406 Å). The specific surface areas of the samples were determined by N<sub>2</sub> adsorption at -196 °C, using the multipoint BET analysis method, with a Micromeritics ASAP-2010 system. The CO chemisorption were measured on a Micromeritics Autochem II chemisorption analyzer for specific surface area of Pt NPs. The chemical elements of Pt/TiO<sub>2</sub> was investigated by X-ray photoelectron spectroscopy (XPS, AXIS-His, KRATOS). X-ray absorption spectroscopy (XAS) was carried out in transmission mode at the 10C beamline of Pohang Light Source (PLS) in the 3.0 GeV storage ring, with a ring current of 70-100 mA. A Si (111) double-crystal was used to monochromatize the X-ray photon energy. The samples were located between the ion chambers. Energy calibration of the Pt L<sub>3</sub>-edge was carried out using Pt foil. X-ray absorption near edge structure (XANES) spectra were recorded for each sample at room temperature using an energy step of 0.2 eV. The obtained data were normalized by Athena software.

### **2.2.3 Electrochemical characterizations**

All electrochemical measurements were performed with standard three-electrode cell. Pt/TiO<sub>2</sub> paste was bladed on FTO glass to form a film, as an

working electrode, a platinum mesh was used as counter electrode and an Ag/AgCl electrode as reference electrode, respectively. 0.1 g of Pt/TiO<sub>2</sub>S were mixed with 0.01 g polyethylene glycol (Fluka), 0.01 g polyethylene oxide (Aldrich), 100  $\mu$ L of acetylacetone ( $\geq$  99%, Sigma-Aldrich) and deionized water. The mixed slurry was bladed onto a 1 x 1 cm<sup>2</sup> area on FTO glass. The blading film was thermally treated at 200 °C for 4 h to remove residual binders. Electrochemical impedance spectroscopy (EIS) measurements were performed on the computer-controlled potentiostat (ZIVE SP2, WonATech). Frequency range EIS experiments were conducted from 1 mHz to 100 kHz under AC stimulus with a 5 mV amplitude under dark condition with applied potential in an electrolyte of 0.5 M NaSO<sub>4</sub>. The impedance data of the equivalent circuit was recorded with ZMAN 2.2 software. The Mott-Schottky plot was exploited from the EIS measurement.

#### **2.2.4 Photoluminescence spectroscopy**

Time-resolved photoluminescence (TRPL) measurements were conducted to investigate decay time of single photon through Fluo-Time 200 instrument (Picoquant, Germany). The excitation is 405 nm pulsed diode laser (pulse energy = 13 pJ, FWHM = 80 ps) with the repetition rate of 80 MHz. The signals were collected from the emission of 1  $\mu$ M rhodamine B (RhB, Sigma). The extinction wavelength ( $\lambda_{em}$ ) was 580 nm. The fitting was evaluated by the reduced  $\chi^2$  value. The fluorescence signal was estimated through an automated motorized monochromator and then collected with a

PicoHarp 300 unit. Data analyses were performed using a PicoQuant Fluofit software program.

### **2.2.5 Photocatalytic performance characterization**

Photoelectrochemical activity was measured by acetaldehyde photodegradation. Test was carried out in a home-made system, and visible light irradiates on samples by 300 W Xe lamp with a 400 nm cut-off filter. The 0.05 g sample was dispersed onto a 1 x 1 cm<sup>2</sup> area of FTO glass in the reactor. The temperature of reactor was maintained at 40 °C by circulating water outside in order to prevent the condensation of an acetaldehyde gas. The injected acetaldehyde was set to 300 ppm by the air gas, which was circulated inside the reactor with closed loop state after acetaldehyde concentration adjusting. Before the photocatalytic activity test, the sample was maintained for 30 min in a dark condition for stabilization. The concentration of degraded acetaldehyde was analyzed using gas chromatography (GC, equipped with a Hydrogen Flame Ionization Detector (FID), Acme6100, Younglin) at 30 min intervals.

## 2.3 Results and discussion

### 2.3.1 Structural characterization

For engineering the Fermi level, Pt nanoparticles (Pt NPs) size was modulated in preparation process. Synthesis of Pt NPs on TiO<sub>2</sub> was conducted by chemical reduction method using NaBH<sub>4</sub>. pH and synthetic temperature were used as factors to control the size of Pt NPs, 1, 3, and 5 nm. The detailed conditions shown in Table 2.1. The electrostatic force is the main factor to explain the synthesis mechanism for size tuning. PtCl<sub>6</sub><sup>4-</sup> precursors were dispersed on negatively charged TiO<sub>2</sub> surface, adjusting to pH 5 in order to obtain smaller Pt NPs. On the other hand, larger size of Pt was synthesized by positively charged TiO<sub>2</sub>, leading to larger Pt NPs. Batch temperatures were controlled from 10 to 60 °C causing a slight aggregation of Pt NPs. Resulting samples were collected by centrifugation, then thermally treated under 10 % H<sub>2</sub>/Ar atmosphere at 300 °C to reduce the remaining oxide species of Pt. Inductively coupled plasma (ICP) analysis was conducted to measure the atomic ratio of Pt NPs in Pt/TiO<sub>2</sub>. Nearly 1 wt% of Pt NPs were deposited on TiO<sub>2</sub> surface (Table 2-2). Morphology and size distribution histograms of Pt nanoparticles in the Pt(x)/TiO<sub>2</sub>s were identified by transmission electron microscope (TEM) analysis in Figure 2.1 and S1. Pt(x)/TiO<sub>2</sub> showed the average diameter to be 1.7, 3.3, and 5.1 nm. Cs-corrected TEM (CS-TEM) images show the crystallinity of exposed Pt nanoparticle (NP) surfaces of Pt(x)/TiO<sub>2</sub>s, which were mainly composed by (111) and (100) surfaces analyzed by the fast Fourier transform (FFT) (Figure

2-2). Ultraviolet-visible diffuse reflectance spectroscopy (UV-Vis DRS), X-ray diffraction spectroscopy (XRD) analysis performed to identify the physicochemical properties of Pt/TiO<sub>2</sub>s. Surface area of Pt/TiO<sub>2</sub> was obtained by Brunauer-Emmett-Teller (BET) and CO adsorption as shown in Figure 2-3 and Table 2-3. In UV-Vis DRS spectra of TiO<sub>2</sub> and Pt(x)/TiO<sub>2</sub>s, it was confirmed that bonding form and interfacial area between Pt and TiO<sub>2</sub> are similar. Bonding form of Pt-TiO<sub>2</sub> interface in the Pt(x)/TiO<sub>2</sub>s were indentified by UV-Vis DRS. Electrons in VB of TiO<sub>2</sub> can absorb the visible light and excited to CB due to rutile TiO<sub>2</sub> has 3 eV bandgap. Main TiO<sub>2</sub> absorbance peak extended and increased absorbance within visible light region (>420 nm) after Pt deposition as shown in Figure 2-3a. Crystal phases of Pt(x)/TiO<sub>2</sub>s and TiO<sub>2</sub> were confirmed by XRD (Figure 2-3b). The rutile phase of TiO<sub>2</sub> were only observed in XRD analysis due to low concentration of deposited Pt NPs. These characterizations clearly indicate that Pt(x)/TiO<sub>2</sub> catalysts were successfully synthesize with various Pt sizes.

### **2.3.2 Eletronic state characterization**

X-ray photoelectron spectroscopy (XPS) and X-ray absorption near edge structure (XANES) were employed to investigate the chemical state and electronic state of Pt NPs in Pt(x)/TiO<sub>2</sub>s (Figure 2-4 and 2-5). In XPS spectra, slight shift toward lower binding energies (BEs) was observed from entire peaks of Pt 4f spectrum due to the electron transfer from TiO<sub>2</sub> to Pt during Fermi level equilibration [32]. Ratio of XPS peak area,  $(Pt^{4+} + Pt^{2+})/Pt_{total}$ ,

was decreased from 0.38, 0.32, and 0.24 in Pt(1), Pt(3) and Pt(5)/TiO<sub>2</sub>. was gradually increased inversely tendency to the size of Pt nanoparticles. Therefore, smaller Pt NPs in the Pt(x)/TiO<sub>2</sub> system obviously received a greater number of electrons from TiO<sub>2</sub> based on XPS measurement.

Scale of charge transfer of junctioned Pt(x)/TiO<sub>2</sub> were investigated by white line intensity comparison in XANES spectra. When visible light (>400 nm) was irradiated and dark condition on Pt(x)/TiO<sub>2</sub> as shown in Figure 2-5. When visible light was irradiated, XANES spectra was shown to be oscillated. This observing oscillation from continuous movement of charge carrier at the Pt(x)/TiO<sub>2</sub> interfaces during equilibration. White line intensity of Pt could decrease if excited electrons in CB of TiO<sub>2</sub> have surplus energy to overcome Schottky barrier under visible light irradiation condition according to reported studies[33,34]. However, white line intensities of Pt(x)/TiO<sub>2</sub> were increase, which means that electrons in Pt NPs seemed to be transferred to CB of TiO<sub>2</sub>. I propose the two possible paths of charge transfer in the Pt/TiO<sub>2</sub> system as follows; i) Hole transfer occurred from TiO<sub>2</sub> VB to Pt after an electron-hole pair formed in TiO<sub>2</sub> by light irradiation. Hole carriers generated by Pt-TiO<sub>2</sub> junction fast and spontaneous move from TiO<sub>2</sub> VB to Pt. ii) Hot electron generating by interband transition at the Pt NPs transport from Pt to TiO<sub>2</sub> CB. In case of Pt, hot electrons were only excited by interband transition, and not by Localized surface plasmon resonance (LSPR). Unlike LSPR in Au, Pt NPs cannot be excited by LSPR due to the insufficient photon energy of visible light for hot electron generation. Au nanoparticles with 2-3 nm act as charge reservoir under only UV light

[35,36], although Au/TiO<sub>2</sub> system was reported including sufficient photocatalytic activity. Thus, 2 nm or less size of noble metal NPs exhibit negligible LSPR [37]. If Pt NPs is excited by LSPR, significantly generate hot electrons and show the electron transfer from Pt to TiO<sub>2</sub> CB, larger Pt NPs show more difference of white line under visible light. Thus, Pt NPs excite the hot electrons by different mechanism of LSPR, which is interband transition [5]. Electrons in Pt 5d band excited to the vacant state of Pt 6sp band existing above the CB of TiO<sub>2</sub> after absorb the visible light. The smaller the size of Pt nanoparticles, the larger the difference of white line intensity after visible light irradiation, which indicates smaller Pt NPs transfer more quantity of electrons to TiO<sub>2</sub> under dynamic equilibrium state. Energy band alignment and kinetic analysis were conducted to prove the hole and electron separation extent and transfer rate at the interface of Pt/TiO<sub>2</sub>.

In Figure 2-6, flat band potentials of Pt(x)/TiO<sub>2</sub>s were estimated by extrapolating the Mott-Schottky plot for the observation of apparent Fermi level. Fermi level of Pt NPs show negative shift with decreasing the Pt size [23]. Faster movement of electron and hole affect on sharper slopes on TiO<sub>2</sub> CB and VB part between the Pt-TiO<sub>2</sub> interfaces due to the higher internal electric field. The sharp slope of Schottky barrier on TiO<sub>2</sub> CB blocks the electron transfer from TiO<sub>2</sub> CB to Pt and allows the fast hot electron transfer from Pt to TiO<sub>2</sub> CB. TiO<sub>2</sub> and Pt(x)/TiO<sub>2</sub>-electrolyte interfaced with  $C_{SC}^{-2}$  and carrier density  $N_D$  are obtained as follows [38,39];

$$\frac{1}{C_{SC}^2} = \left( \frac{2}{e\epsilon\epsilon_0 N_D} \right) \left[ (V - V_{fb}) - \frac{k_B T}{e} \right] \quad (1)$$

$$N_D = \frac{2}{e\epsilon\epsilon_0} \left[ \frac{d(1/C_{SC}^2)}{dV} \right]^{-1} \quad (2)$$

Where  $V_{fb}$  is flat band potential,  $V$  is applied potential,  $\epsilon_0$  is vacuum permeability,  $\epsilon$  is dielectric constant of electrode material and  $e$  is elementary charge. Flat band potential ( $V_{fb}$ ) can be elucidated from x-intercept according to the equation (1).  $V_{fb}$  of Pt(x)/TiO<sub>2</sub>s were increased as decreasing the size of Pt NPs compared to bare TiO<sub>2</sub>. Carrier density ( $N_D$ ) can be estimated from the inverse slope of Mott-Schottky plot as in the equation (2). Pt/TiO<sub>2</sub> with smaller Pt NPs exhibited higher  $N_D$  value. Calculated  $N_D$  of Pt(1), Pt(3), and Pt(5)/TiO<sub>2</sub> were  $5.99 \times 10^{19}$ ,  $3.82 \times 10^{19}$ , and  $3.43 \times 10^{19} \text{ cm}^{-3}$  as  $\epsilon$  value was obtained from literature[40]. It was identified that  $N_D$  was increased according to the size decrement of Pt NPs, which indicates the increased amount of charge separation between Pt(x)-TiO<sub>2</sub> interface with small x value. The larger amount of charge separation indicates wider depletion region and higher electric field in the TiO<sub>2</sub> material, which was thought to be from Fermi level modulation in accordance with the sizes of Pt NPs. Furthermore, the tendency of apparent Fermi level shift is similar to the variation amount of white line intensities in XANES spectra before and after light irradiation, which empowers the charge separation mechanism by composited electron and hole transport in the Pt/TiO<sub>2</sub> system under visible light as shown in Figure 2-7.

Hole transfer rate constant from TiO<sub>2</sub> valence band to Pt confirmed that the opposite sign but same magnitude to electron transfer rate constant from TiO<sub>2</sub> conduction band to Pt when a product of charge carrier concentration is constant under experimental condition as follows (Figure 2-8);

$$N_T \cdot P_T = N_c N_v e^{-(E_c - E_{Fc})/k_B T_c - (E_{Fv} - E_v)/k_B T_v} = C \text{ (const.)}$$

When hole concentration variation is considered from Figure 2-8,

$$\frac{dP_T(t)}{dt} = -k_{T \rightarrow P}^+ P_T(t),$$

where  $-k_{T \rightarrow P}^+$  is hole transfer rate constant. From the conservation of product between two types of carrier concentrations,  $P_T(t)$  can be

expressed as  $P_T(t) = \frac{C}{N_T(t)}$ . When the above hole carrier concentration

variation equation was substituted to electron carrier concentration:

$$\frac{dP_T(t)}{dt} = C \cdot \frac{d}{dt} \left( \frac{1}{N_T(t)} \right) = C \cdot \frac{dN_T(t)}{dt} \cdot \frac{(-1)}{\{N_T(t)\}^2} = -k_{T \rightarrow P}^+ P_T(t) = -k_{T \rightarrow P}^+ \frac{C}{N_T(t)},$$

$$\frac{dN_T(t)}{dt} = k_{T \rightarrow P}^+ N_T(t),$$

$$\frac{dP_T(t)}{dt} = -k_{T \rightarrow P}^+ P_T(t) \leftrightarrow \frac{dN_T(t)}{dt} = k_{T \rightarrow P}^+ N_T(t)$$

Therefore, it was identified that variation of hole concentration in the TiO<sub>2</sub> valence band makes variation of electron concentration in the TiO<sub>2</sub> conduction band by opposite way, which was indicated by scheme in Figure 2-9c.

### 2.3.3 Photoluminescence characterization

Figure 2-9 represents a Time-resolved photoluminescence (TRPL) results to estimate the charge carrier dynamics and kinetic processes of charge transport in the Pt/TiO<sub>2</sub> systems. Synthesized samples were suspended in a rhodamine B with excitation spectrum of 405 nm [41-43]. Excited electrons from RhB are transferred to TiO<sub>2</sub> or Pt/TiO<sub>2</sub> system, which form electron transfer path in the photocatalytic system. An electron transfer rate constant from Pt to TiO<sub>2</sub> and a hole transfer rate constant from TiO<sub>2</sub> to Pt were fitted from multi-exponential model considering the overall electron transfer path. TPRL analysis was used to explain a charge transfer path in aspects of electron as shown in Figure 2-9c. Hole transfer from TiO<sub>2</sub> VB to Pt seemed to be contradicted at intuitive aspect, however, electron and hole carrier concentration is conserved in the same temperature under thermodynamically aspects. Hole transfer rate from TiO<sub>2</sub> VB to Pt constant was mathematically calculated using the electron transfer rate from TiO<sub>2</sub> CB with opposite sign (Figure 2-8). Figure 2-10a shows the two operating types of charge transfer processes under visible light irradiation condition. electron-hole carrier was separated by visible light excitation on either Pt or rutile TiO<sub>2</sub>. Separated holes of rutile TiO<sub>2</sub> transport from TiO<sub>2</sub> VB to Pt, while electrons were blocked by high Schottky barrier. Electrons in Pt 5d band was excited by interband transition, which directly transfer Pt to TiO<sub>2</sub> CB. Thus, charge transfer kinetic was analyzed fully in the aspect of electron

transfer path. electron and hole transfer rates were obtained, considering the net electron transfer from Pt to TiO<sub>2</sub> CB.

Measured time-resolved spectra were fitted to the sum of two individual single exponential decays described as;

$$I(t) = \sum_{i=1}^2 A_i e^{-\frac{t}{\tau_i}} \quad (3)$$

where  $\tau_i$  is the decay time and  $A_i$  represents the amplitude of the components at  $t=0$ . The emission of RhB was expressed by a one exponential function and that of TiO<sub>2</sub> also by the other exponential function. All of the fitted kinetic parameters are included in the supporting information (Table 2-4). Overall charge transfer path and charge transfer rate constants from calculation are listed in Figure 2-9c, Figure 2-10b and Table 2-5. The electron transfer rate from Pt to TiO<sub>2</sub> CB was obtained using decay time of RhB. The hole transfer rate from TiO<sub>2</sub> VB to Pt was solved and calculated by substituting that to the congruence electron transfer rate based on PL of TiO<sub>2</sub>. Overall charge transfer rate constants were calculated and included in Table 2-6. The electron transfer rate ( $k_{R \rightarrow P \rightarrow T}$ ) from Pt and the hole transfer rate ( $k_{T \rightarrow P}^+$ ) from TiO<sub>2</sub> was rapidly decreased when the size of Pt NPs in Pt(x)/TiO<sub>2</sub> was increased, mainly due to the formation of larger electric field formation between Pt-TiO<sub>2</sub> interface with lower apparent Fermi level.

### 2.3.4 Photooxidation reactivity

In figure 2-11, gaseous acetaldehyde photocatalytic oxidation reaction was investigated in to determine the effect hole site generation on Pt NPs and

charge separation on Pt(x)/TiO<sub>2</sub>s under visible light ( $\lambda > 400$  nm). Charge carriers were excited simultaneously at the TiO<sub>2</sub> VB and Pt NPs and consequently electron accumulation on TiO<sub>2</sub> CB and hole on Pt NPs. Acetaldehyde photodegradation could be from both charge carriers. Holes on Pt NPs could directly oxidize acetaldehyde molecule. Electrons on TiO<sub>2</sub> CB could convert oxygen to superoxide anion, which sequentially degrades acetaldehyde (Figure 2-12). Pt(x)/TiO<sub>2</sub>s show better performance than bare TiO<sub>2</sub>, resulting from interfacial charge separation at the Pt(x)/TiO<sub>2</sub>s interface. As shown in 2-10a, the decreasing rate of acetaldehyde were 0.359, 0.239, and 0.197 h<sup>-1</sup> for Pt(1), Pt(3), and Pt(5)/TiO<sub>2</sub>. It means that the activities of Pt(x)/TiO<sub>2</sub>s were gradually increased with decreasing Pt size. However, higher performance of Pt(x)/TiO<sub>2</sub> with smaller Pt NPs could also be believed to be come from higher external Pt surface area. If photocatalytic performance comes not from interfacial charge transfer but from high external surface area, Pt(x)/TiO<sub>2</sub> system with smaller Pt NPs should also show better performance in the dark condition, since external metal surface cannot be related with interfacial charge separation. The degradation rates of acetaldehyde on TiO<sub>2</sub> and Pt(x)/TiO<sub>2</sub>s showed a reverse tendency compared to light condition, which decrease in the order of TiO<sub>2</sub>, Pt(5), Pt(3), and Pt(1). It implies that the photocatalytic performance is not affected by external surface area. This reverse result could be from more electron accumulation in the Pt part of Pt(x)-TiO<sub>2</sub> interface with smaller x value during Fermi level equilibration, due to the lower initial Fermi level of smaller Pt NPs. Therefore, charge separation by hole transfer in the Pt-TiO<sub>2</sub> interface could

be more dominant than external surface area effect. The electron transfer rate constants ( $k_{R \rightarrow P \rightarrow T}$ ), the hole transfer rate constants ( $k_{T \rightarrow P}^+$ ) and acetaldehyde photooxidation rates are listed in Figure 2-13. Larger amount of hole site conservation on Pt NPs from recombination ensures faster oxidation of reactant. When the electron transfer from Pt to TiO<sub>2</sub> CB and the hole transfer from TiO<sub>2</sub> VB to Pt were increased, acetaldehyde conversion rates were also similarly increased as anticipated. Drastic increase of reactivity was observed in Pt(1)/TiO<sub>2</sub>, in common with rapid increment of the charge transfer rate and amount in Pt(1)/TiO<sub>2</sub>.

**Table 2-1.** The pH and temperature condition to control the size of Pt(x)/TiO<sub>2</sub>.

Entry	pH	Temperature (°C)
Pt(1)/TiO <sub>2</sub>	5	10
Pt(3)/TiO <sub>2</sub>	3	50
Pt(5)/TiO <sub>2</sub>	1	60

**Table 2-2.** Concentration of Pt in Pt(x)/TiO<sub>2</sub> analyzed by ICP analysis.

Entry	Pt amount (wt %)
Pt(1)/TiO <sub>2</sub>	0.9618
Pt(3)/TiO <sub>2</sub>	1.0232
Pt(5)/TiO <sub>2</sub>	1.0625

**Table 2-3.** Surface area of Pt(x)/TiO<sub>2</sub> and Pt(x) based on BET and CO adsorption analysis.

Entry	Surface area of Pt(x)/TiO <sub>2</sub> by BET (m <sup>2</sup> /g-catal)	Surface area of Pt(x) by CO adsorption (m <sup>2</sup> /g-metal)
TiO <sub>2</sub>	38.92	-
Pt(1)/TiO <sub>2</sub>	40.00	21.53
Pt(3)/TiO <sub>2</sub>	36.36	11.97
Pt(5)/TiO <sub>2</sub>	35.62	5.51

**Table 2-4.** Kinetic parameters elicited from results of time-resolved PL spectra of 1  $\mu$ M RhB in the presence of samples with 405 nm excitation.

Entry	$A_1$	$\tau_1$ (ns)	$A_2$	$\tau_2$ (ns)	$\chi^2$
Rhodamine B	12213	1.44	-	-	0.985
TiO <sub>2</sub>	10226	1.412	80.7	3.025	0.969
Pt(1)/TiO <sub>2</sub>	10317	1.313	77.3	3.908	0.985
Pt(3)/TiO <sub>2</sub>	10618	1.376	61.5	3.522	0.972
Pt(5)/TiO <sub>2</sub>	11809	1.395	59.6	3.41	0.982

**Table 2-5.** Solving processes of governing equation, analytical solutions, and electron transfer rate constants in the RhB solution, TiO<sub>2</sub> in the RhB solution, and Pt(x)/TiO<sub>2</sub> in the RhB solution. Hole transfer rate constants was especially considered in the Pt(x)/TiO<sub>2</sub> system.

System	Governing equation and solution	Charge transfer rate constants
RhB solution	(i) $\frac{dN_R}{dt} = -k_R N_R$ $\rightarrow N_R = N_{R0} e^{-k_R t}$	$k_R = \frac{1}{\tau_{1,RhB}}$
TiO <sub>2</sub> + RhB solution	(i) $\frac{dN_R}{dt} = -(k_R + k_{R \rightarrow T}) N_R$ $\rightarrow N_R = N_{R0} e^{-(k_R + k_{R \rightarrow T}) t}$ (ii) $\frac{dN_T}{dt} = k_{R \rightarrow T} N_R - k_T N_T$ $\rightarrow N_T = C_1 e^{-(k_R + k_{R \rightarrow T}) t} + C_2 e^{-k_T t}$	$k_{R \rightarrow T} = \frac{1}{\tau_{2,TiO_2}} + \frac{1}{\tau_{1,RhB}}$ $k_T = \frac{1}{\tau_{2,TiO_2}}$
Pt(x)/TiO <sub>2</sub> + RhB solution	(i) $\frac{dN_R}{dt} = -(k_R + k_{R \rightarrow T} + k_{R \rightarrow P \rightarrow T}) N_R$ $\rightarrow N_R = N_{R0} e^{-(k_R + k_{R \rightarrow T} + k_{R \rightarrow P \rightarrow T}) t}$ (ii) $\frac{dN_T}{dt} = k_{R \rightarrow T} N_R - (k_T - (-k_{T \rightarrow P})) N_T$ $= k_{R \rightarrow T} N_R - (k_T -$	$k_{R \rightarrow P \rightarrow T} = \frac{1}{\tau_{1,Pt(x)/TiO_2}} + \frac{1}{\tau_{1,TiO_2}}$ $k_{T \rightarrow P}^+ = -k_{T \rightarrow P}$ $= -\frac{1}{\tau_{2,Pt(x)/TiO_2}} + \frac{1}{\tau_{2,TiO_2}}$

$$k_{T \rightarrow P}^+ N_T$$

→

$$N_T$$

$$= C_3 e^{-(k_R + k_{R \rightarrow T} + k_{R \rightarrow P \rightarrow T})t}$$

$$+ C_4 e^{-(k_T - (-k_{T \rightarrow P}))t}$$

$$= C_3 e^{-(k_R + k_{R \rightarrow T} + k_{R \rightarrow P \rightarrow T})t}$$

$$+ C_4 e^{-(k_T - k_{T \rightarrow P}^+)t}$$

$$C_1 = \frac{k_{R \rightarrow T}}{k_T - (k_R + k_{R \rightarrow T})} \cdot N_{R0} \quad C_3 = \frac{k_{R \rightarrow T}}{(k_T + k_{T \rightarrow P}) - (k_R + k_{R \rightarrow T} + k_{R \rightarrow P \rightarrow T})} \cdot N_{R0}$$

$$C_2 = N_{T0} - C_1$$

$$C_4 = N_{T0} - C_3$$

**Table 2-6.** Charge transfer rate constants of TiO<sub>2</sub> and Pt(x)/TiO<sub>2</sub>s Obtained from fitted results of time-resolved PL spectra according to solving processes.

Entry	$k_R$ ( $10^8 \text{ s}^{-1}$ )	$k_T$ ( $10^8 \text{ s}^{-1}$ )	$k_{R \rightarrow P \rightarrow T}$ ( $10^8 \text{ s}^{-1}$ )	$k_{T \rightarrow P}^+$ ( $10^8 \text{ s}^{-1}$ )
TiO <sub>2</sub>			-	-
Pt(1)/TiO <sub>2</sub>	0.69473	0.33058	0.05328	0.07469
Pt(3)/TiO <sub>2</sub>			0.01818	0.04655
Pt(5)/TiO <sub>2</sub>			0.00828	0.03732

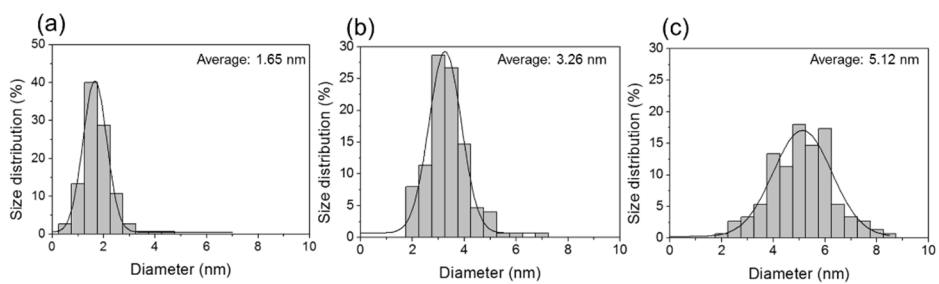


**Figure 2-1.** Pt NP size distributions of Pt(x)/TiO<sub>2</sub>s with each x value of (a) 1, (b) 3, and (c) 5.

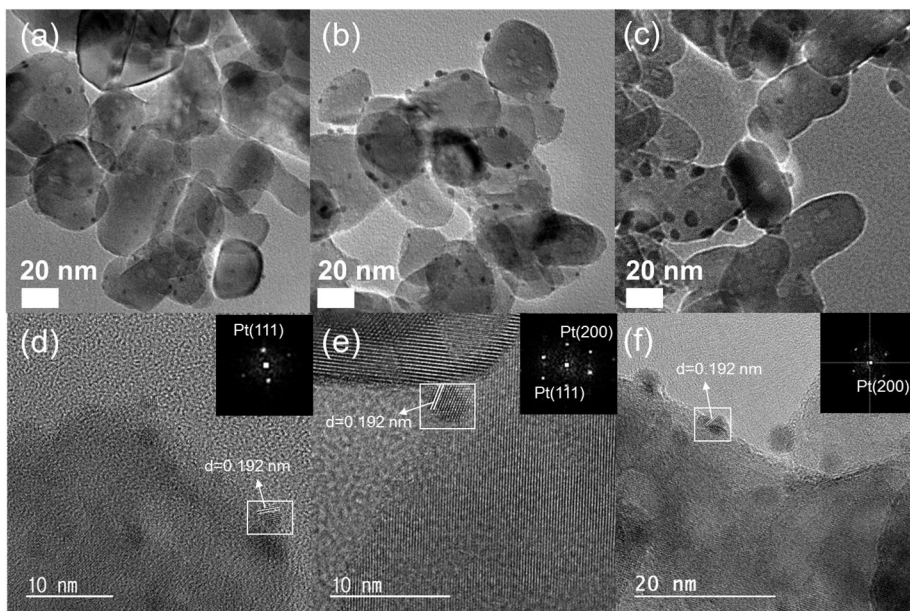


**Figure 2-2.** TEM images and Cs-TEM images of Pt(1)/TiO<sub>2</sub>, Pt(3)/TiO<sub>2</sub>, and Pt(5)/TiO<sub>2</sub>. Each x value in Pt(x)/TiO<sub>2</sub>s is corresponding to an average Pt NP size. FFT patterns were obtained from a Pt NP in Cs-TEM images.

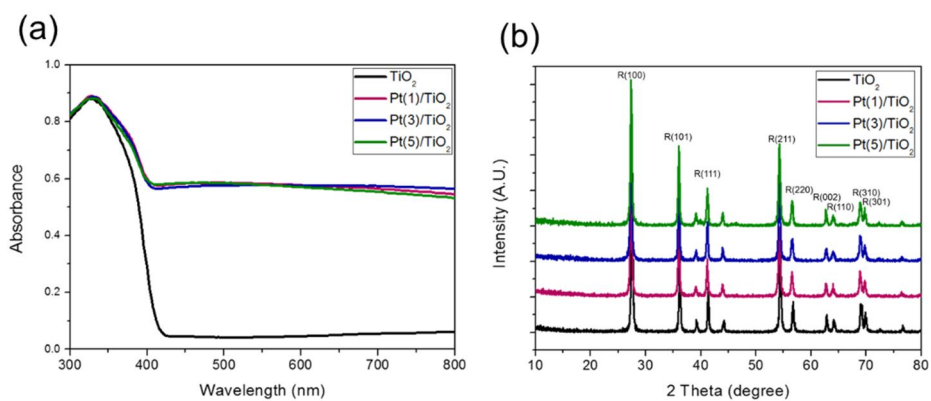


**Figure 2-3.** Physicochemical characterization results of TiO<sub>2</sub> and Pt(x)/TiO<sub>2</sub> as a function of Pt NP size by (a) UV-Vis-DRS and (b) XRD analysis.

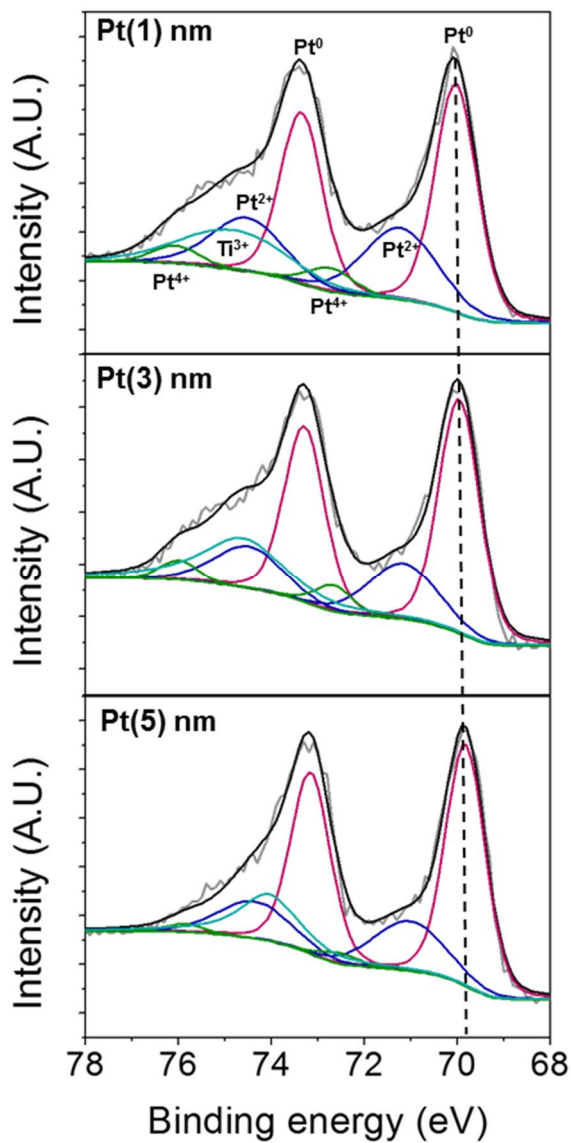


**Figure 2-4.** Pt 4f XPS spectra of Pt(x)/TiO<sub>2</sub>s. Binding energies was red-shifted compared to generally known values due to strong M-S interaction.

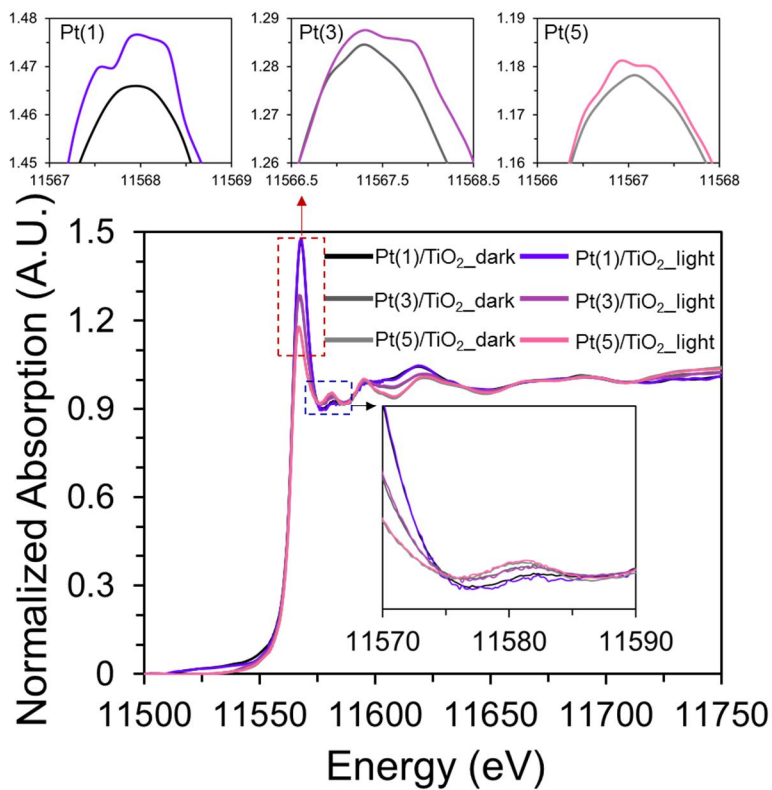


**Figure 2-5.** Pt L3 edge XANES spectra of Pt(x)/TiO<sub>2</sub>s in the light on/off. The enlarged insets show the difference of white line intensity of Pt(x)/TiO<sub>2</sub>s (red) and the blue indicate an oscillation parts (blue).

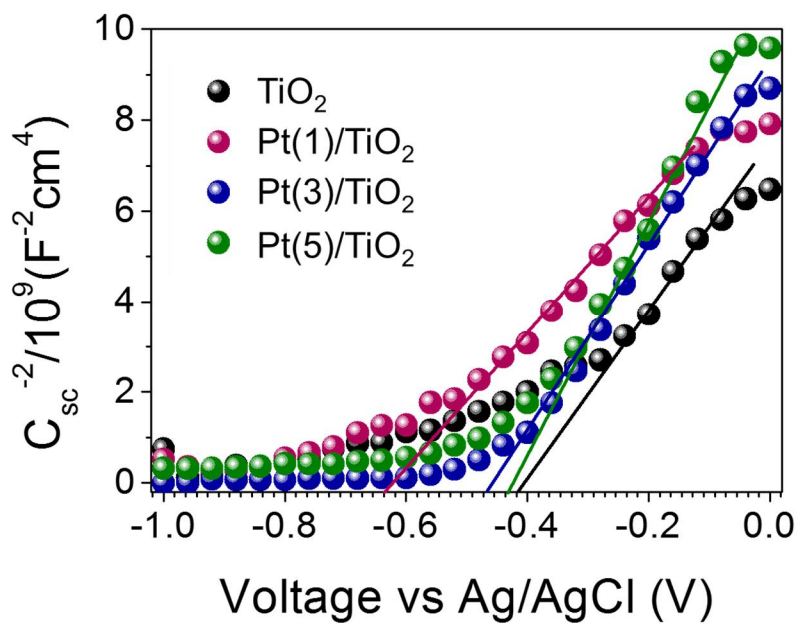


**Figure 2-6.** Mott-Schottky plot of  $TiO_2$  and Pt(x)/ $TiO_2$ s under dark condition.

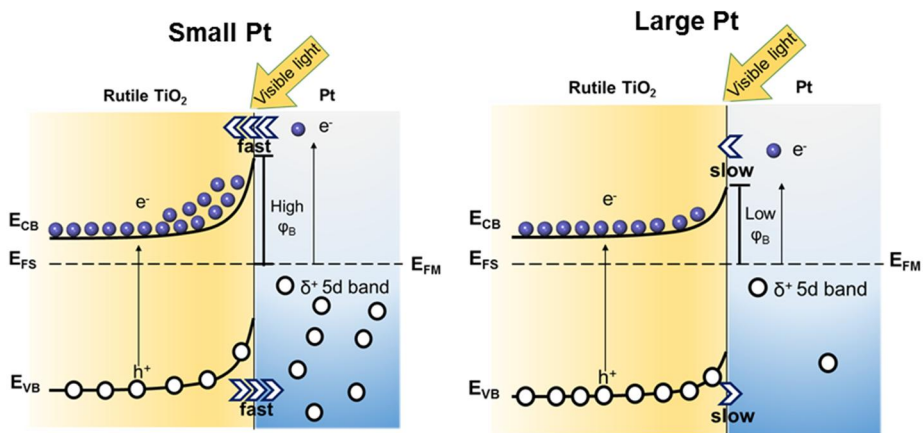


**Figure 2-7.** Schematic diagrams for representing charge flows of Pt/TiO<sub>2</sub> systems with Pt NP size under visible light irradiation condition.

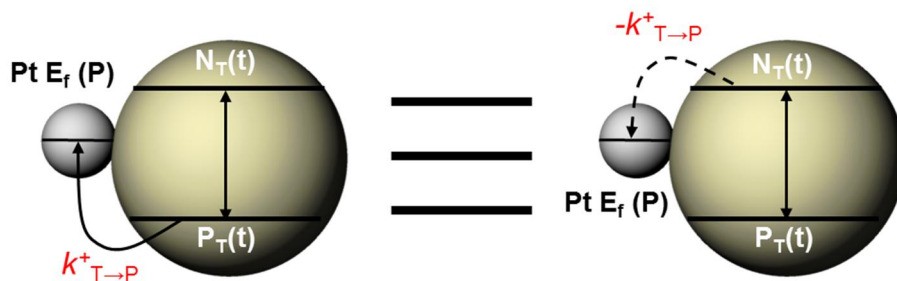


**Figure 2-8.** Schematic diagram explains the in the aspects of kinetics. When electron and hole carrier concentration thermodynamically remains constant, electron transfer from TiO<sub>2</sub> CB to Pt ( $-k_{T \rightarrow P}^+$ ) can be considered as hole transfer from TiO<sub>2</sub> VB to Pt ( $k_{T \rightarrow P}^+$ ) according to the mathematic calculation.

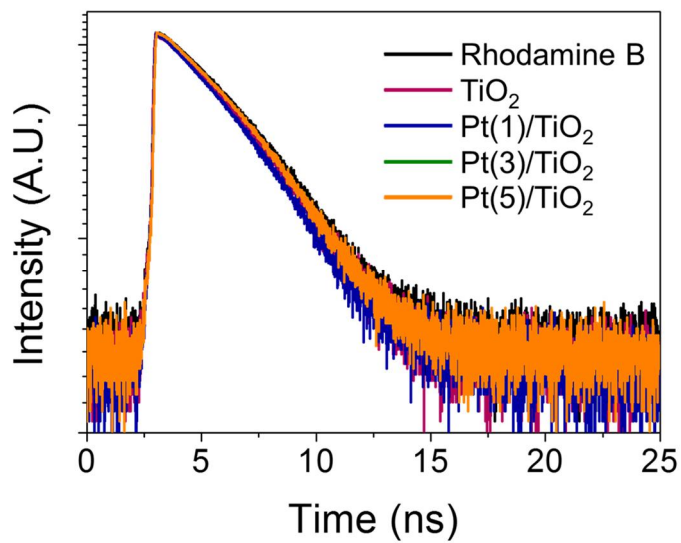


**Figure 2-9.** Time-resolved photoluminescence spectra (TRPL) of TiO<sub>2</sub> and Pt(x)/TiO<sub>2</sub>s with 405 nm laser excitation where emission wavelength was 580 nm in the 1  $\mu$ M RhB solutions.

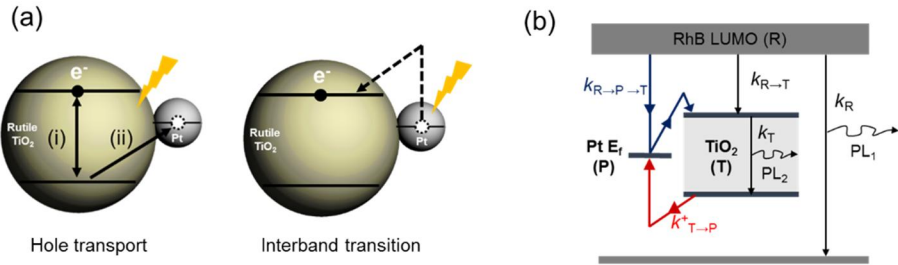


**Figure 2-10.** (a) Schematic diagram of Pt(x)/TiO<sub>2</sub>s charge transfer path under visible light excitation. Hole transport is caused by semiconductor excitation, and electron transport is directly induced by metal excitation. (b) Schematic energy band diagram of charge transfer path of Pt/TiO<sub>2</sub> results from the time-resolved PL measurement. Electron transfer rate constants are indicated as black and blue arrows, and a hole transfer rate as red arrows.

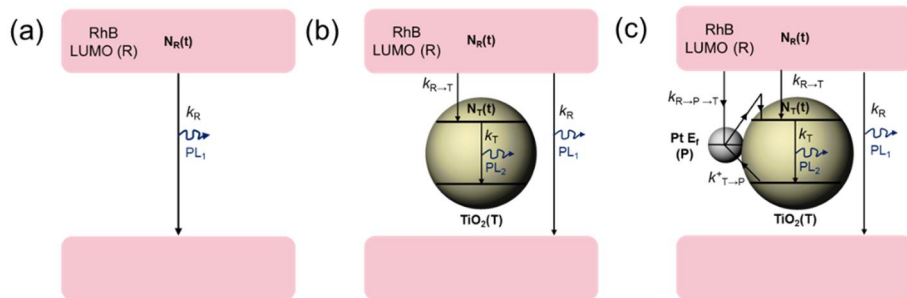


**Figure 2-11.** (a) Schematic charge transfer path under visible light excitation in the (a) RhB, (b) TiO<sub>2</sub> in RhB, and (c) Pt(x)/TiO<sub>2</sub> in RhB.

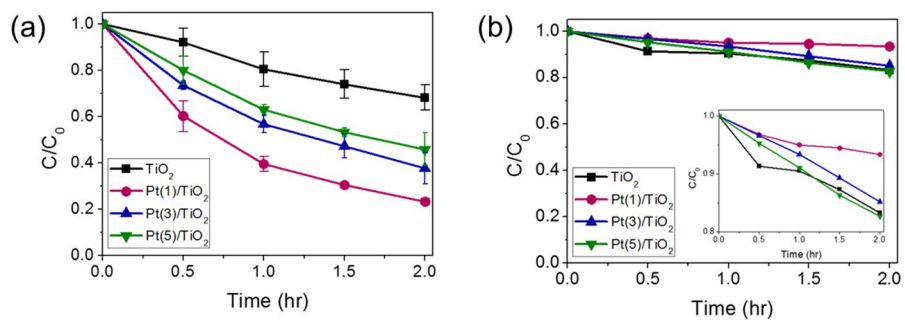


**Figure 2-12.** Acetaldehyde photodegradation of  $\text{Pt}(x)/\text{TiO}_2$  under (a) visible light irradiation (>400 nm) and (b) and enlarged inset shows the photocatalytic rate under dark condition.

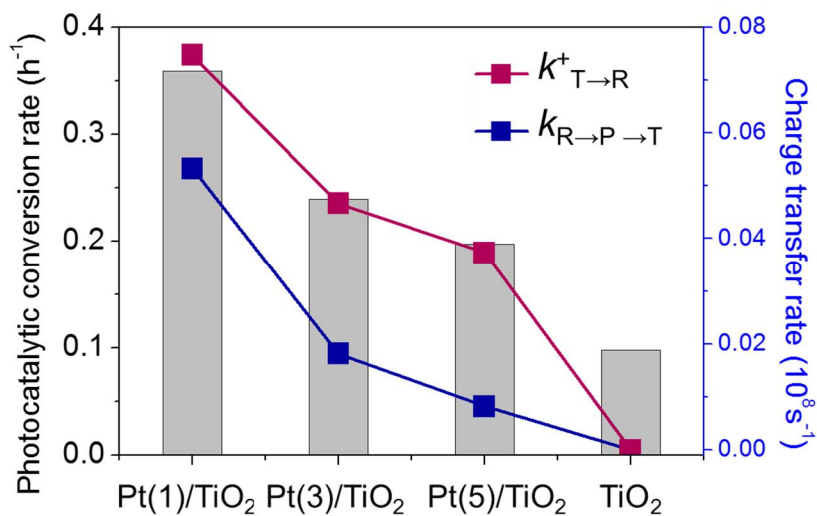


**Figure 2-13.** The acetaldehyde photocatalytic rate and charge separation constants. Acetaldehyde conversion rates are as denoted by gray bar. Red line indicates the hole transfer rate ( $k^+_{\text{T} \rightarrow \text{P}}$ ) and blue line show the electron transfer rate ( $k_{\text{R} \rightarrow \text{P} \rightarrow \text{T}}$ ).

# **Chapter 3. Tuning the photonic crystal nanostructure for guiding of visible light**

## **3.1 Introduction**

Morpho butterflies are well known for the brilliant blue color in their wings. This unique color has been shown on the surface of wings which are composed of periodically arranged cuticle layers. This phenomenon is called a structural color [44,45]. The structural color originates from a combination of several optical properties such as constructive interference at multilayer [46], diffraction at grating surface [47], and light scattering in the irregular structure with different refractive indices. Photonic crystals have been regarded as promising material leading a structural color by controlling photonic bandgap (PBG)[48]. When light propagates through the periodic structure, the certain wavelength of light is confined in the PBG for producing a structural color in the visible light region [49]. The way to produce unique coloration through photonic crystal has been received a lot of interest due to potential platform for enhancing the visible light harvesting [50]. Therefore, recent studies have shed light on the optical application of photonic crystals due to diversity of material, superior optical excellency and chemically-stable properties compared to pigmentary treatments which suffer from photobleaching problems [51,52].

A design of structural color through photonic crystal has been achieved at diverse dimensions. First, Bragg stacks or Bragg reflectors are the simplest model of 1D photonic crystals. This planar structures are composed of multilayers of alternate high- and low-refractive index film [53,54]. Second, 2D arranged metal nanowires (NWs) or nanotubes (NTs) with structural color are fabricated from the metallic substrate by just varying transverse size and gap of the structures [55-58], allowing for possible integration with other electronic and optical circuits. However, these 1D and 2D photonic crystals require complex and high-cost instruments to tune the arrangement. Lastly, 3D photonic crystals, colloidal opal or inverse opal, have the ability to manipulate light more efficiently than 1D or 2D photonic crystals because morphologies (e.g.; size, symmetry, and defects) of 3D photonic crystals are controlled by simple treatments on a large scale. In particular,  $\text{TiO}_2$  is one of the most appropriate material for photonic crystals which are prepared from self-driven approach of opal or inverse opal structure become useful method to generate structural color due to low-cost, wide tunability, and high chemical and mechanical stability [59]. However, stability of  $\text{TiO}_2$  photonic crystals still remains a challenge to large scale production because of weak physical contact with substrate from the existence of cracks [60-62]. To overcome the limitation for generation of 2D photonic crystal,  $\text{TiO}_2$  nanotube array (TNA) is a good candidate for visible light utilization due to high surface area, mechanical strength, and high refractive index. There are only few studies about photonic crystals coloration method through using  $\text{TiO}_2$

nanotube in spite of its superior chemical stability and cost-effective manner [63]

Herein, we mimic the wings of butterfly with structural color from  $\text{TiO}_2$  nanotube array through controlling the geometry including cell thickness and pore diameter by two-step anodizing. Structural periodicity and refractive index of TNA play an important role in generation of structural color. Bragg's equation is used to predict the reflectance peak of TNA based on the diffractive light as considering the geometry and refractive index of medium [57,64]. An art image was printed on the TNA surface through anodizing for optical printing application [65]. The replicated image shows that fabricating a large-scale painting represents a high resolution image that it can be alternated to pigments painting without the complicated process. TNA film has advantages that it shows high-resolution under the irradiation of light or exposure to organic solvents despite ultrathin and light weight. Generated structural color of TNA and fundamental aspect which principle of color change depends on the refractive index and periodicity of structure can be used for various optical applications [66].

## **3.2 Experimental**

### **3.2.1 Fabrication of 2D TiO<sub>2</sub> photonic crystals**

A high-purity Ti foil (99.7%, 0.127 mm thickness, Sigma-Aldrich) was cut into 1 cm × 4 cm sections. The Ti sheets were degreased by sonicating in acetone, ethanol, and deionized water (DI water) in sequence. A Ti sheet was used as an anode with a Pt mesh as a cathode in a two-electrode system where the electrolyte consisted of 97 vol% of ethylene glycol (99.9%, Samchun), 3 vol% DI water, and 0.3 wt % NH<sub>4</sub>F (≥98.0 %, Sigma-Aldrich). The Ti sheet was first anodized using a variety of voltages (30, 40, 50, 60, 65, and 75 V) for 1 h using DC power supply (PAP-3001, Powertron). The oxidized layer was then completely removed by using a sticky tape and ultrasonication. The second anodization was performed under the same conditions as the first anodizing process for 240 s (at 30 V), for 180 s (at 40 V), for 120 s (at 50 V), for 90 s (at 60 V), for 50 s (at 65 V), and for 40 s (at 75 V) to obtain more stable and uniform structure. The temperature was maintained at 15 °C by circulating a coolant through an external temperature-control device during the anodizing processes.

### **3.2.2 Characterization**

The morphology and size of the resulting films were observed using a field emission scanning electron microscope (FE-SEM, Sigma, Carl Zeiss). The reflectance spectra were obtained by an ultraviolet-visible diffuse reflectance

spectroscopy (UV-DRS, V670, Jasco).

### **3.2.3 Color printing using a 2D TiO<sub>2</sub> photonic crystals**

A Ti foil was cut into 10 cm X 8 cm sheets, and a sketch of the original painting was drawn on the Ti sheet. Before the anodizing step, all parts of the Ti sheet were coated with an insulating adhesive, nitrocellulose layer, except for the areas to be colored. The layer acts as a protective coat which inhibits the infiltration of electrolyte. This makes it possible to achieve the selective anodization of uncoated sections. The exposed sections of the Ti sheet were first anodized at a certain voltage for 1 h, followed by the elimination of the oxidized layers, as described above. In turn, the neighboring sections were subjected to a second anodization at the same voltage for the corresponding time. And then, the coating layer was removed by acetone and water. The other colors were also printed on the Ti sheet in the same way.

### **3.2.4 Photoelectrochemical water splitting**

To enhance the photocatalytic efficiency, TNA was made with two-layer. After 2<sup>nd</sup> anodization, sonication for 5 min was applied to TNA for removing the partial TNA from the surface. 3<sup>rd</sup> anodization was performed at the different voltage to extend the absorbing range of visible light. Before Au nanoparticles were deposited on TNA with structural color, TNA was annealed at 450 °C for 4 h. crystallinity of TNA changes from amorphous to anatase phase to apply the photocatalytic electrode. HAuCl<sub>4</sub> act as a precursor, and

thermal reduction method was used to form the Au nanoparticles on TNA. 0.1 mM HAuCl<sub>4</sub> solution was dropped to TNA surface with spin coater at 1000 rpm to 10 seconds. Au/TNA was dewetted under 10 % H<sub>2</sub>/Ar atmosphere for 300 °C for 3 h to reduce the Au ions.

The photocurrent performance of Au/TNA was evaluated under chopped light irradiation using a three electrode system with the Pt mesh as a counter electrode, and Ag/AgCl electrode act as a reference electrode in 0.5 M Na<sub>2</sub>SO<sub>4</sub> solution. 300 W Xe lamp was used as a light source including UV and visible light. Light on/off cycle is 30 seconds at a fixed electrode potential at 0 V. Photocurrent activity measurements were conducted on the computer-controlled potentiostat (ZIVE SP2, WonATech).

## 3.3 Results and discussion

### 3.3.1 Characterization

The procedure for fabricating the TiO<sub>2</sub> nanobowl arrays is illustrated in Figure 3-1. A thin Ti foil was first anodized at a certain potential in the range of 30–75 V to produce TiO<sub>2</sub> nanotubes with different diameters. The rough and irregular TiO<sub>2</sub> nanotubes were completely removed using a sticky tape and ultrasonication, leaving a hexagon-shaped concavity pattern on the surface of the Ti foil. The pretreated Ti foil was anodized a second time at the same potential applied as was used in the first anodization step for several seconds, consequently forming hierarchical TiO<sub>2</sub> nanobowl arrays. It should be noted that the imprinted pattern that remained after the first anodization plays a crucial role in determining the diameter of the nanobowls. TiO<sub>2</sub> nanobowl arrays were prepared a total of three times for checking the reproducibility of this process. Field emission scanning electron microscope (FESEM) images in Figure 3-2 show the top view of the as-prepared TiO<sub>2</sub> nanobowl arrays, in which the average diameter gradually increases from 41 nm to 106 nm with increasing applied potential: 30, 40, 50, 60, 65, and 75 V (Figure 3-3). The porous nanobowl arrays display structural color that strongly depends on the diameter of air cavity and thus shifts from indigo to red. The height of each TiO<sub>2</sub> nanobowl was around 100 nm in all of the arrays (Figures 3-4). The thickness of the resulting TiO<sub>2</sub> nanobowl structures was sufficiently thin to generate light reflection from the bottom plane that served as a mirror layer in order to increase the scattering intensity of the

normal incident light. However, if the height is too high, the film reflects white color due to multiple scattering [61,67,68]. That is, a thick PhC causes incoherent and multiple scattering of the incident light and then results in a low chroma of the structural color.

Figure 3-5 shows the measured optical reflection spectra where the as-synthesized TiO<sub>2</sub> nanobowl arrays exhibit two separated peaks; one narrow reflection peak and the other a broad reflection band. As the diameter of air cavity is increased from 41 to 106 nm, the two reflection peaks were linearly red-shifted and their full-width at half-maximum (FWHM) gradually increased. In particular, these characteristics were prominently featured in the broad reflection band as compared to a relatively narrow reflection peak, contributing to the interval between the two peaks to become wider. The corresponding optical image for each sample was given as the inset along with the reflection curve. The color gradually changed from indigo to red with increasing cavity diameter. Note that two different reflection peaks emanate from the flat bottoms and inclined planes of the cavity [8,69,70]. Lights reflected from the sides are visible to the bare eyes, while the reflection at the center or bottom is dissipated. Specifically, the incident light on the sides of the cavity is retro-reflected due to double reflection, and the polarization of the reflected light is then rotated upon each reflection.

### **3.3.2 Modified Bragg diffraction theory**

The structural color change of the TiO<sub>2</sub> nanobowl arrays was predictable

through light diffraction and refraction theories, as schematically illustrated in Figure 3-6. When light of a specific wavelength,  $\lambda$ , is incident on a regularly arranged structure with spacing  $d$ , the light is scattered along a lattice direction. If the scattered waves constructively interfere with each other, the path difference between two waves is equal to an integer multiple of the radiation wavelength. The Bragg's law derived from the constructive interference can be combined with Snell's law of refraction, and the resulting

equation is given by, 
$$m\lambda = n_{\text{eff}}d(\sin\theta_i - \sin\theta_r) \quad (1)$$

where  $m$  is the order of diffraction,  $\theta_i$  is the incident angle,  $\theta_r$  is the reflected angle, and  $n_{\text{eff}}$  is the mean effective refractive index. The  $n_{\text{eff}}$  depends on the porous structure of the TiO<sub>2</sub> nanobowl arrays, and defined as following equation [45],

$$n_{\text{eff}} = \sqrt{fn_1^2 + (1-f)n_2^2} \quad (2)$$

where  $n_1$  is 1 for the refractive index of the air,  $n_2$  is 2.49 for the amorphous TiO<sub>2</sub>, and  $f$  is the volume fraction of pore [71]. The  $f$  can be determined from the  $d$  and wall thickness,  $w$ , of the TiO<sub>2</sub> nanobowl.

$$f = 1 - \frac{2\pi w(w+d)}{\sqrt{3}(2w+d)^2} \quad (3)$$

If the incident light is directly reflected ( $\theta_i = \theta_r$ ), this is called the Littrow configuration [72-74]. Then, Equation (1) changes to,

$$m\lambda = 2d \cdot n_{\text{eff}} \sin\theta_r \quad (4)$$

This model can describe how the TiO<sub>2</sub> nanobowl arrays reflect light of certain wavelengths. The reflected wavelengths can be calculated using the

above equations, and the values are summarized with the parameters in Table 3-1. The calculated wavelengths also gradually increased with increasing diameter of cavity, and the values were consistent with the experimentally reflected wavelengths. Although there are two variables, diameter and refractive index that can change the reflected wavelength, a change in diameter has much more influence on the reflectance of PhCs than that of the refractive index [11,75].

### **3.3.3 Color Printing**

Color printing applying a structural color on a thin metal substrate has a high resistance to bleaching by sunlight and toxic solvents as compared to conventional methods for color generation using pigments or dyes [76]. Plasmonic materials can be used for color printing, based on surface plasmon resonances resulting from the oscillation of electrons between metal and dielectric interfaces [77]. However, producing patterns using photonic crystals or plasmonic materials with distinct colors remains a challenge because low reflectivity and diffraction-limitations are drawbacks to plasmonic color system. In order to enhance the reflectivity, a metal film or a metal oxide film can be used to obtain high reflectivity as spacer layer leading to an increase in the cost and process step. The fabrication method introduced in this study was extended to a centimeter scale through a facile, quick, and cost-effective process. We reproduced a Mondrian painting known as ‘Composition with Color Planes and Gray Lines’ on a 10 cm X 8

cm Ti sheet of without any complex architectures. It should be noted that this color shift allows one to print arbitrary features with complex and multiple length scales. Each color in the original painting shown in Figure 3-7a was produced by hierarchical arrays of the bowl structure with different diameters which were systemically designed from the modified Bragg's equation instead of a trial-and-error method for the production of the desired colors. Consequently, they display a similarity to the original colors, and the distinct colors showed a fine contrast and brightness in the reproduced painting (Figure 3-7b). This result suggests that the anodization method for a color printing can be a promising method to produce structural colors. The corresponding nanostructure for each color was further highlighted in a high magnification image of some selected areas (Figure 3-7.c-f), which illustrated different diameters and a uniform alignment of the nanobowls.

The fabrication process allows a flexible design of printed images on a thin metal sheet and the colors are chemically/mechanically stable in a harsh environment for a long time, unlike chemical dyes or 3D photonic crystals. A peel test was performed on the TiO<sub>2</sub> nanobowl arrays to examine the mechanical stability of the nanostructure by attaching and detaching a section of Scotch tape over the film where the tape has an adhesive strength to metal of 2.5 N/cm (Figure 3-8). The findings indicated that the TiO<sub>2</sub> nanobowl arrays not only maintained their distinct colors and the nanostructure was preserved even under repetitive testing. The stability of structural color of the TiO<sub>2</sub> nanobowl arrays was compared with a conventional pigment-derived color under the irradiation of lights. The

structural color was well maintained under the irradiation by direct sunlight or fluorescent light (Figure 3-9), while a N3 dye, a standard ruthenium-complex dye for dye-sensitized solar cells, was not stable on the commercial TiO<sub>2</sub> nanoparticles, P25, due to the oxidative degradation of the dye. The fluorescent light contains a negligible UV, indicating that N3 dye does not undergo photocatalytic degradation by the excitation of P25 with a wide bandgap. The wavelength shift for the N3 absorption is caused by molecular deformation through a photosensitization process. In addition, when the TiO<sub>2</sub> nanobowl arrays were immersed in various solvents such as NaCl, HNO<sub>3</sub>, NaOH, ethanol, acetone, benzene, and toluene, respectively, they remained stable. Figure 3-10 shows the stability of TiO<sub>2</sub> nanobowl arrays after being exposed to diverse stimulus. Although the refractive index is a variable that can cause a change in the reflected wavelength, the relative change in diameter is usually much more significant than the refractive index [54, 78]. This method has great promise for practical applications including producing anti-counterfeit tags, wearable sensors, and displays. This system can be also combined with noble metal clusters or photoactive molecules for the photoelectrochemical conversion of hydrocarbons or producing H<sub>2</sub> from water.

### **3.3.4 Photoelectrochemical water splitting**

Photoelectrochemical (PEC) water splitting under visible light is studied for hydrogen generation, considering the charge separation, light harvesting and

photostability. TNA with structural color can be used to photoelectrochemical cell due to several advantages. First, TiO<sub>2</sub> channel shows the property of 1D nanostructures such as nanorods, nanofibers, and nanotubes, which provide efficient electron-hole pair pathways compared to 3D particles exhibiting the carrier recombination at grain boundaries [79,80]. Therefore, TNA with permanent color is suitable for employing on PEC applications.

Figure 3-11 represents dual-layer TNA and Figure 3-12 show the Au NPs coated on the TNA surface. Dual-layer TNA was composed of top and bottom layer with different pore diameter. As above mentioned, the absorbance range of visible light was determined by pore diameter of TNA. TNA with multi-layer including different pore diameter can trapped more visible light region compared to single layer which has the single absorbance peak as shown in Figure 3-13(a) from UV-vis DRS. Dual-layer TNA was rationally designed to match the photonic bandgap and LSPR region of Au. In XRD spectra, Au/TNA exhibits the anatase phase while TNA before thermal treatment show the titanium peak. Au peak was not observed due to lower loading amount.

To evaluate the enhanced photoelectrochemical performance of Au/dual-layer TNA, photocurrent test was performed under 300 W Xe lamp at an applied potential 0 V (Figure 3-14). The photocurrent density of TNA show little photocurrent density close to 0 mA/cm<sup>2</sup>. The photonic bandgap of TNA can not activate by light irradiation because TNA has the amorphous structure. The photonic bandgap of TNAG is matched with LSPR peak of Au

within 500 nm while TNAR show different photonic bandgap region. The photocurrent density enhancement was observed on the Au/TNAG from LSPR enhancement than Au/TNAR. In case of Au/Dual TNA, three times of photocurrent density was evaluated from multiple scattering of light of TNA photonic structure [81]. Therefore, hot electron excited by Au contribute to the enhancement photocurrent density when photonic bandgap of TNA and LSPR peak of Au were overlapped.

**Table 3-1.** Structural parameters and reflection wavelengths of the synthesized TiO<sub>2</sub> nanobowl arrays with different colors

Entry	$w$ (nm)	$d$ (nm)	$\lambda_c$ (nm) <sup>a</sup>	$\lambda_m$ (nm) <sup>b</sup>
Indigo	35 ± 0.6	41 ± 3.2	325	361 ± 3.2
Blue	47 ± 4.6	52 ± 5.6	432	434 ± 10.2
Green	55 ± 0.6	61 ± 5.1	506	514 ± 11.4
Yellow	61 ± 2.1	83 ± 1.7	600	599 ± 12.4
Orange	66 ± 0.6	92 ± 9.8	654	677 ± 10.1
Red	67 ± 4.6	106 ± 7.8	695	707 ± 9.3

<sup>a</sup>  $\lambda_c$  is the calculated peak wavelength.

<sup>b</sup>  $\lambda_m$  is the measured peak wavelength.

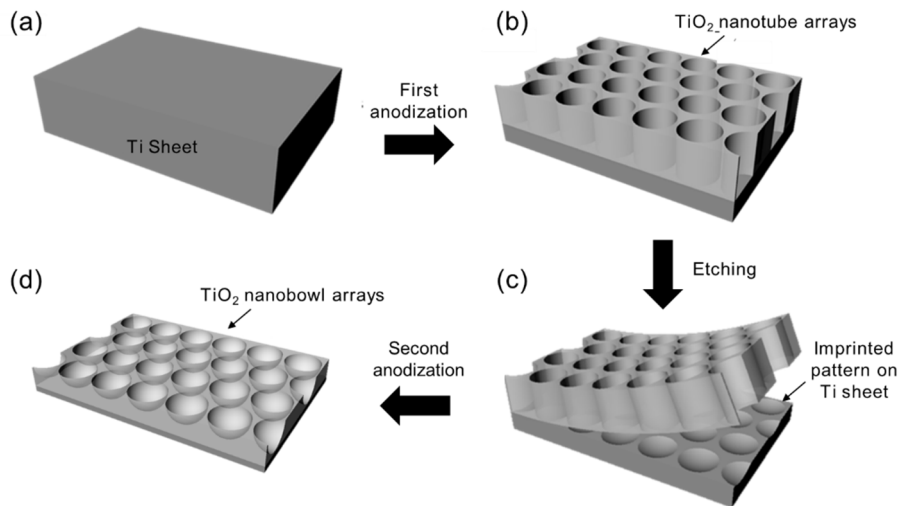


**Figure 3-1.** A schematic diagram of the fabrication of  $\text{TiO}_2$  nanobowl arrays with a structural color. (a) A Ti sheet was prepared as a source of  $\text{TiO}_2$ . (b)  $\text{TiO}_2$  nanotubes are formed on the Ti sheet through first anodization step. (c) The oxide layer was removed by using a sticky tape and ultrasonication leaving a hexagonal concave pattern on the Ti sheet. (d)  $\text{TiO}_2$  nanobowl arrays with a structural color were fabricated by applying anodizing potential for several seconds.

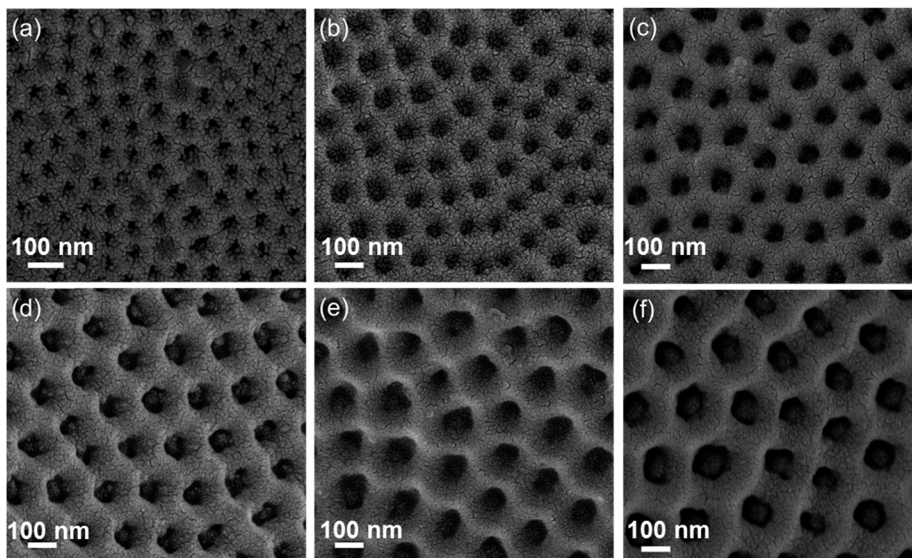


**Figure 3-2.** SEM images of TiO<sub>2</sub> nanobowl arrays with different diameters of air cavities that prepared by altering anodizing potential: (a) 30 V, (b) 40 V, (c) 50 V, (d) 60 V, (e) 65 V, and (f) 75 V. Scale bars indicate a length of 100 nm.

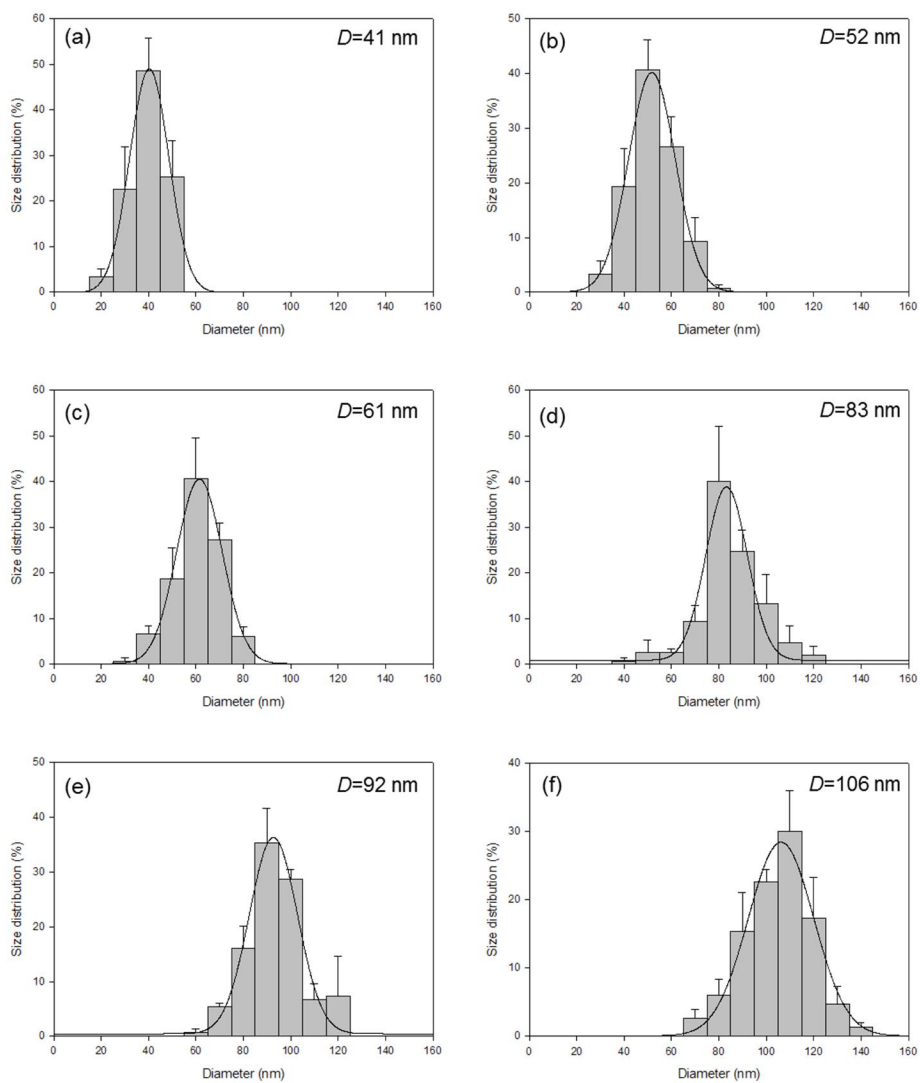


**Figure 3-3.** Size distribution histograms of TiO<sub>2</sub> nanobowl arrays that prepared by altering anodizing potential: (a) 30 V, (b) 40 V, (c) 50 V, (d) 60 V, (e) 65 V, and (f) 75 V.

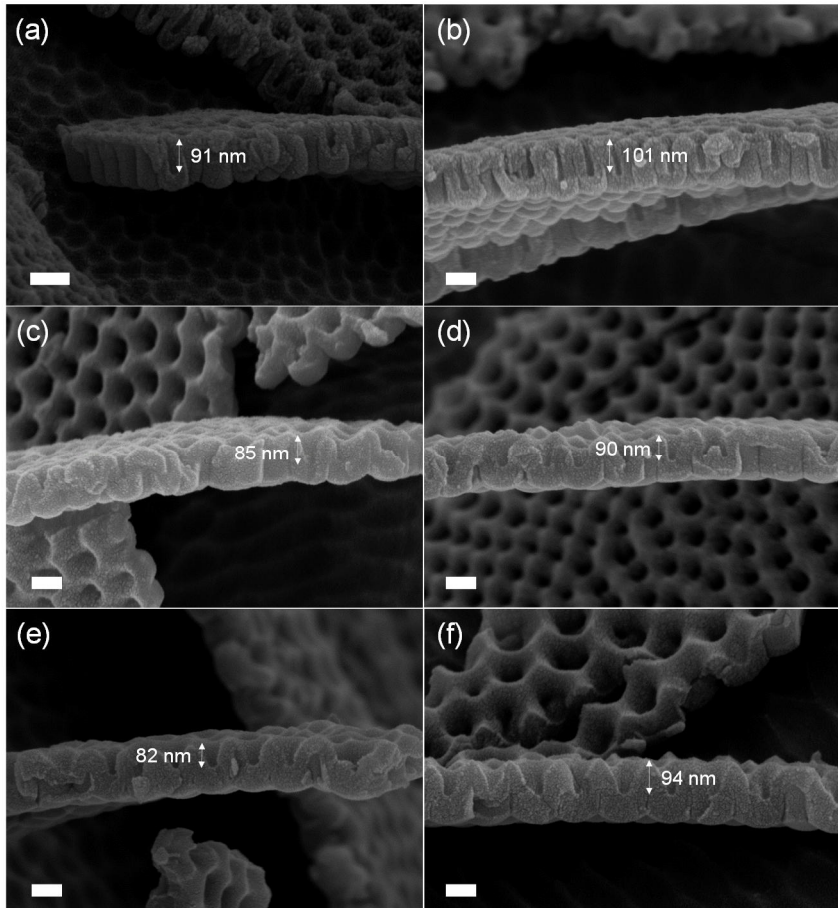


**Figure 3-4.** Cross-sectional SEM images of TiO<sub>2</sub> nanobowl arrays which were fabricated at anodizing conditions of (a) 30 V, (b) 40 V, (c) 50 V, (d) 60 V, (e) 65 V, and (f) 75 V. Scale bars indicate a length of 100 nm.

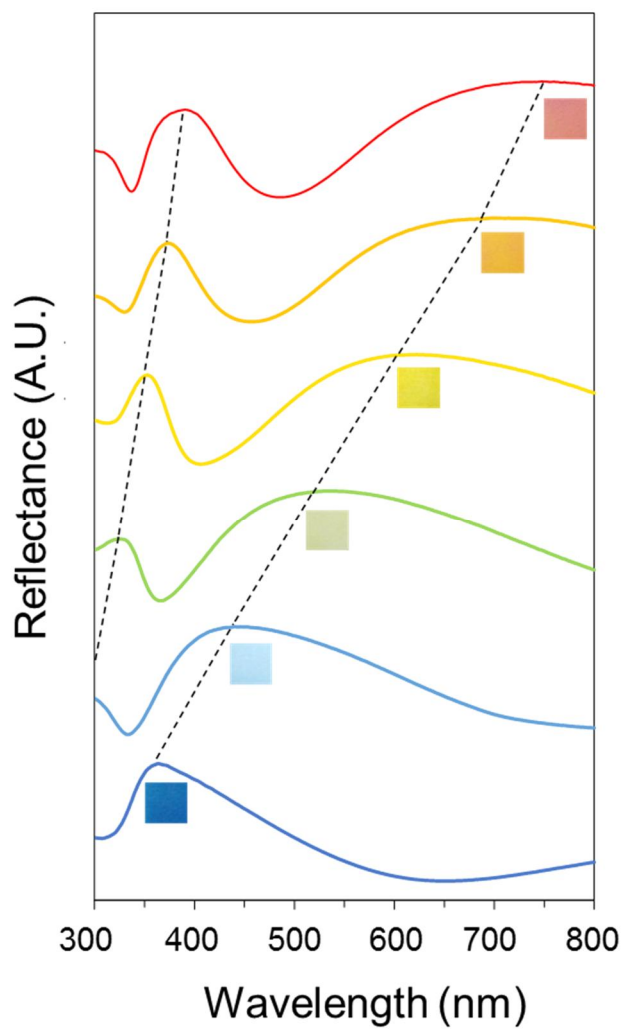


**Figure 3-5.** Reflectance spectra of TiO<sub>2</sub> nanobowl arrays with different diameter air cavities. The trend (dotted) lines approximate the shift of the peaks with increasing diameter of the nanostructures.

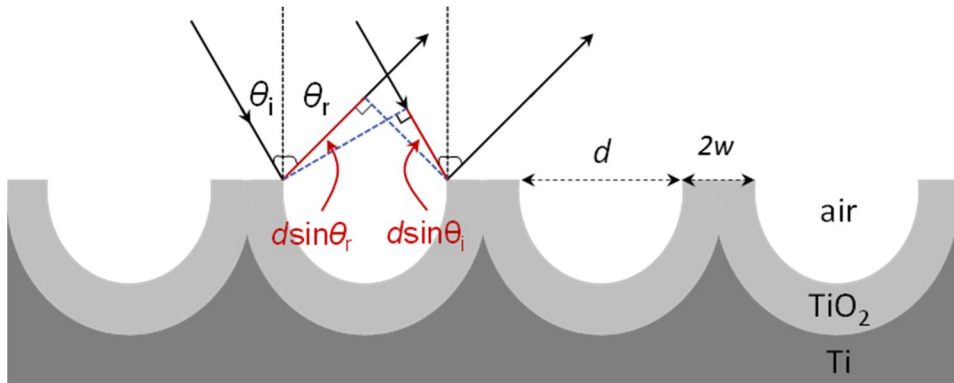


**Figure 3-6.** The reflection path of incident light on the TiO<sub>2</sub> nanobowl structure followed by modified Bragg diffraction theory.

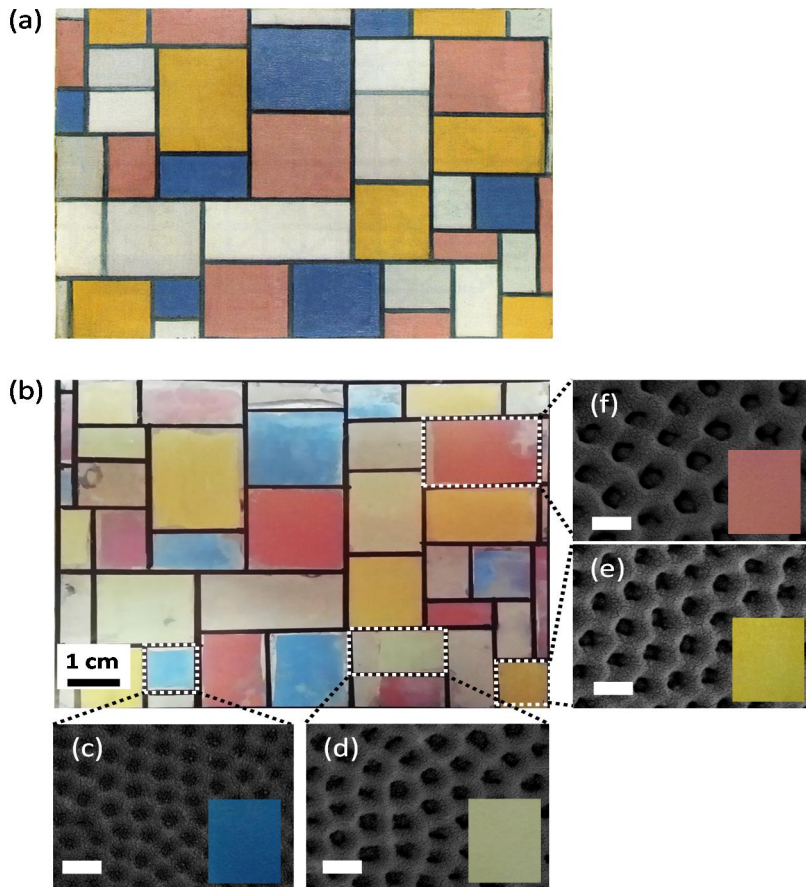


**Figure 3-7.** (a) A Mondrian painting known as *Composition with Color Planes and Gray Lines*. (b) The reproduced image on a centimeter scale. (c–f) SEM images of selected areas, which illustrate different diameters and uniform alignment of the nanobowls. White scale bar indicates a length of 200 nm.

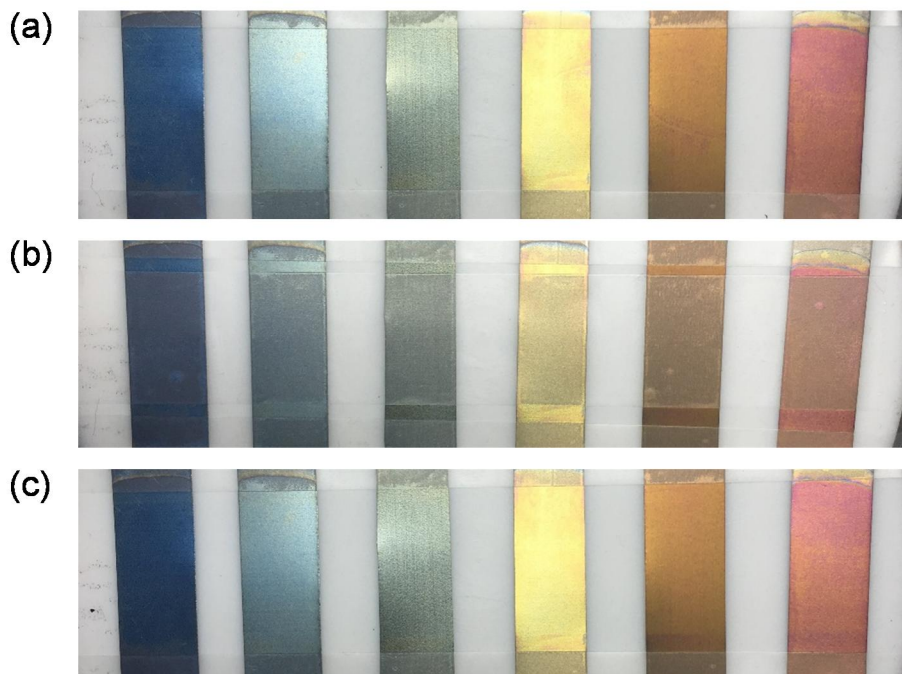


**Figure 3-8.** Adhesion tape peeling test to analyze the mechanical stability of  $\text{TiO}_2$  nanobowl arrays: (a) before the attachment of a tape, (b) a tape attached on the  $\text{TiO}_2$  nanobowl arrays, and (c) after the detachment of the tape from the  $\text{TiO}_2$  nanobowl arrays.

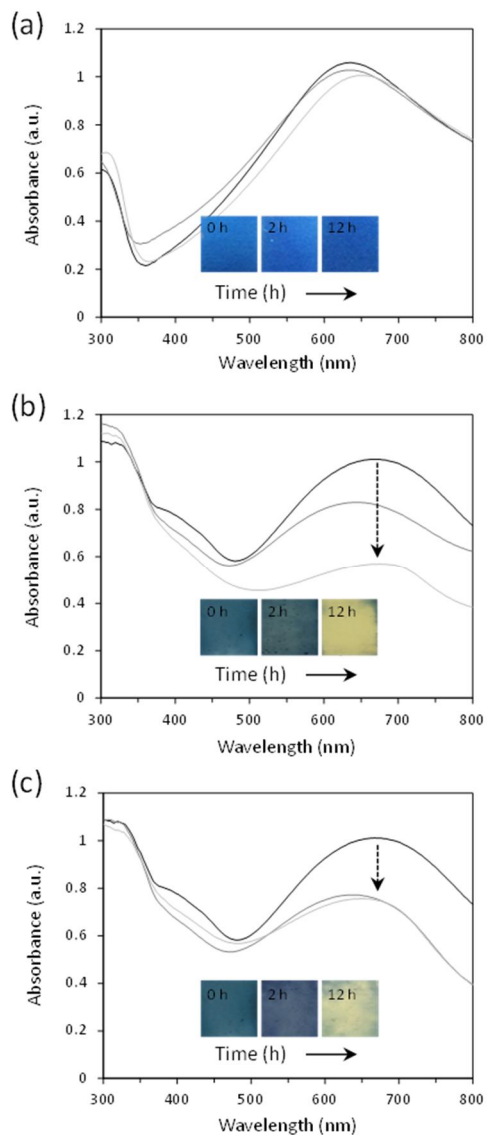


**Figure 3-9.** UV-vis absorbance change of (a) TiO<sub>2</sub> nanobowl arrays with a blue color and (b) a N3 dye coated on the P25 under irradiation by direct sunlight, and (c) N3 dye coated on the P25 under irradiation of fluorescent light for 12 h. Insets are images taken during the stability test.

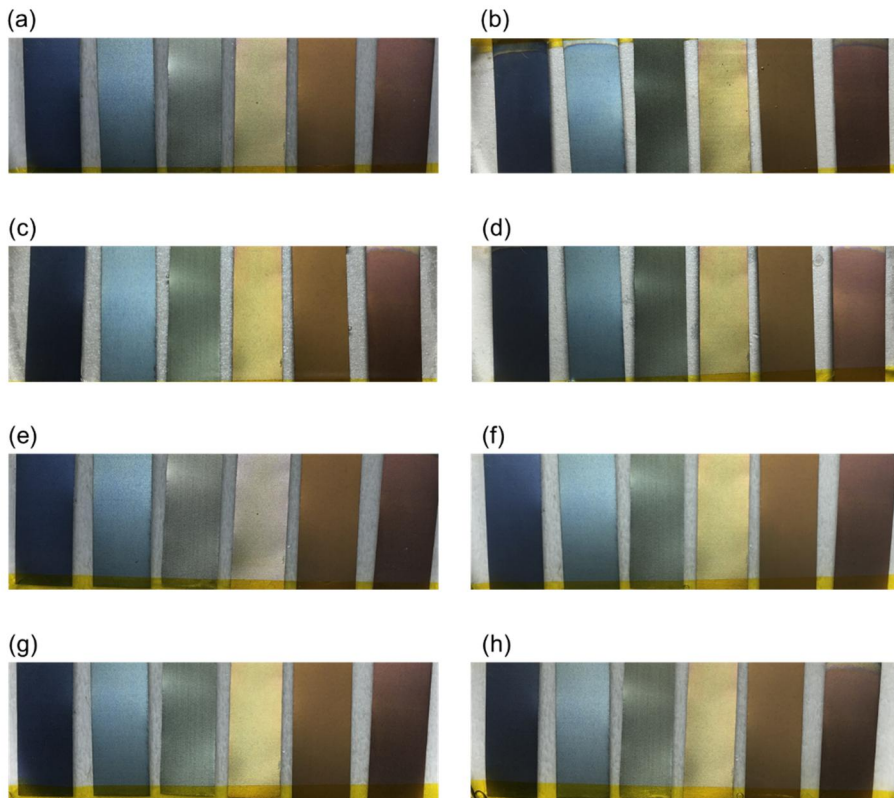


**Figure 3-10.** TiO<sub>2</sub> nanobowl arrays immersed in various solvents; (a) water, (b) 1 M NaCl, (c) 1 M HNO<sub>3</sub>, (d) 1 M NaOH, (e) ethanol, (f) acetone, (g) benzene, and (h) toluene.

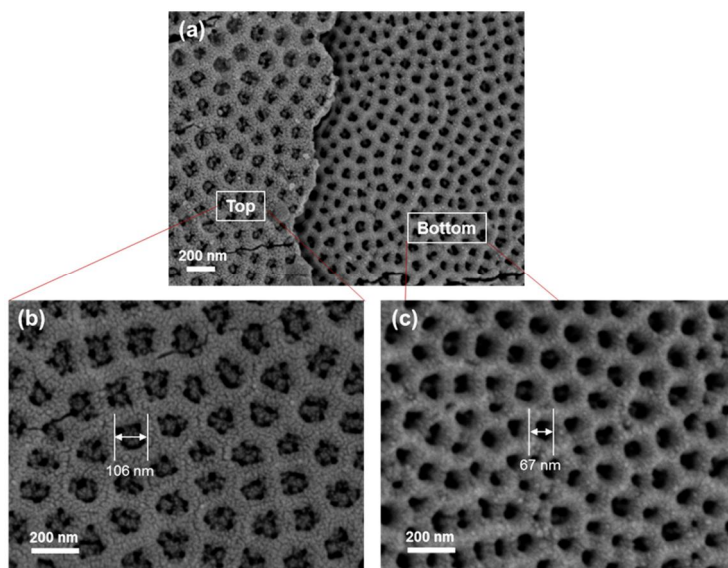


**Figure 3-11.** SEM images of TiO<sub>2</sub> nanobowl arrays with (a) different diameters, (b) top layer including about 106 nm pore size and (c) 67 nm.

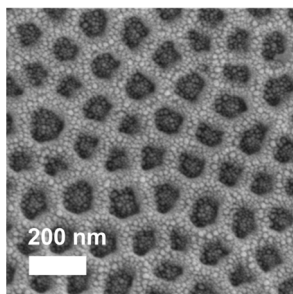


**Figure 3-12.** FE-SEM images of Au nanoparticles deposited on TNA surface.

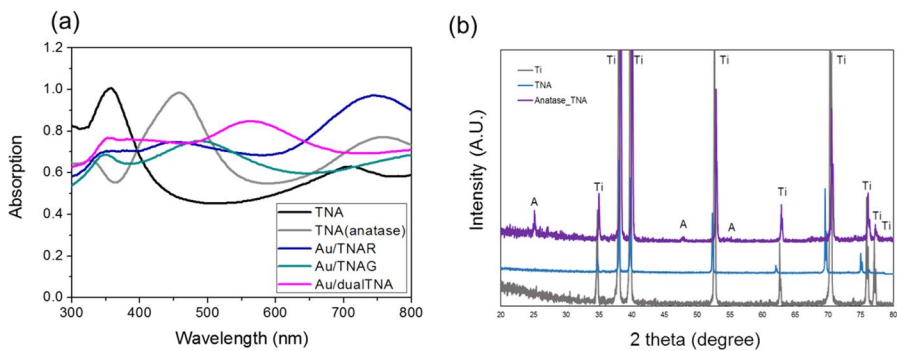


**Figure 3-13.** Physicochemical characterization results of TNA, annealed TNA, Au/TNAR, Au/TNAG, Au/dual TNA analyzed by (a) UV-vis DRS and (b) XRD.

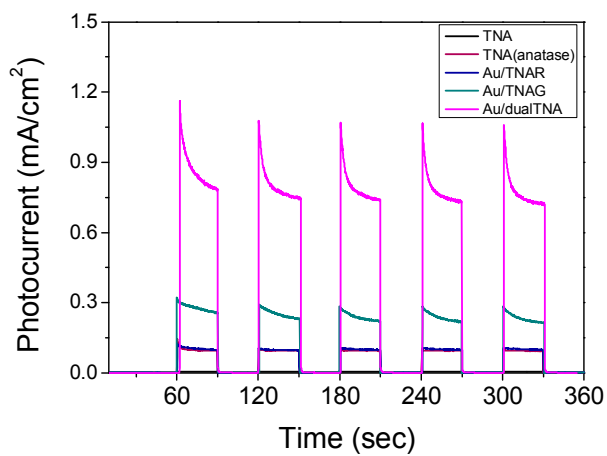


**Figure 3-14.** Photocurrent density in the 0.5 M Na<sub>2</sub>SO<sub>4</sub> electrolyte at an applied potential of 0 V under light irradiation with 30 s light on/off cycles.

## Chapter 4. Summary and Conclusions

As one of the strategies for enhancing the absorption the visible light of photocatalysts,

modulation of electron and hole transfer extent was investigated both in energetic and kinetic aspects. Selected Pt/TiO<sub>2</sub> systems with adjustable apparent Fermi levels by size variable control of supported Pt NPs. charge separation pathway was suggest by synergetic electron and hole transfer mechanism under visible light region. When Fermi level gets lower in the Pt/TiO<sub>2</sub> system, larger electric field on TiO<sub>2</sub> VB and CB induces faster and greater amount of hole transfer from TiO<sub>2</sub> VB to Pt and electron transfer from Pt to TiO<sub>2</sub> CB. The amount and rate of compositive electron and hole transfer were directly related to the photocatalytic performance in the hole mediated acetaldehyde photooxidation reaction. This report will contribute to the rational design of multicomponent photocatalytic system in the energetic alignment aspect.

Strucutural modulation is another strategie that control the matrial property to guiding light;

2D TiO<sub>2</sub> photonic crystals produce variable structural colors inspired Morpho-butterfly. Hierarchical TiO<sub>2</sub> nanobowl arrays were fabricated by a two-step anodization process where the nanobowl structure brought about two different reflection peaks from its flat bottom and inclined plane. The positions of the two reflection peaks as well as their wavelength gap can be

simply adjusted by changing the diameter of TiO<sub>2</sub> nanobowls that are dependent on the anodizing potential. The reflected wavelength gradually increased with changing the periodicity of the TiO<sub>2</sub> nanobowl, as expected from Bragg diffraction theory. This method enabled a broad color distribution with a high contrast and brightness to be created without employing complicated color generation. Also, combined photonic nanostructure with metal nanoparticles was supported to enhance the LSPR. Light trapping in TNA structure amplificate the hot electron formation at Au metal. This work contributes to the ratioanl design of visible-light responsive based on photonic band gap engineering for photoelectrochemical applications.

## Bibliography

- [1] M. R. Gholipour, C.-T. Dinh, F. B'eland and T.-O. Do, *Nanoscale*, **2015**, 7, 8187–8208
- [2] A. Jujishima and K. Honda, *Nature* **1972**, 238, 37-38.
- [3] Y. Lu, H. Yu, S. Chen, X. Quan and H. Zhao, *Environ. Sci. Technol.* **2012**, 46, 1724-1730.
- [4] P. V. Kamat, *J. Phys. Chem. Lett.* **2012**, 3, 663-672.
- [5] J. Li and N. Wu, *Catal. Sci. Technol.* **2015**, 5, 1360–1384.
- [6] G. Liu, H. G. Yang, J. Pan, Y. Q. Yang, G. Q. Lu and H.-M. Cheng, *Chem. Rev.* **2014**, 114, 9559–9612.
- [7] Q. Weng, Y. Ide, X. Wang, X. Wang, C. Zhang, X. Jiang, Y. Xue, P. Dai, K. Komaguchi, Y. Bando and D. Golberg, *Nano Energy*, **2015**, 16, 19–27.
- [8] Y. Y. Diao, X. Y. Liu, G. W. Toh, L. Shi and J. Zi, *Adv. Funct. Mater.* **2013**, 23, 5373–5380.
- [9] J. Zi, X. Yu, Y. Li, X. Hu, C. Xu, X. Wang, X. Liu and R. Fu, *Proc. Natl. Acad. Sci. U. S. A.* **2003**, 100, 12576–12578.
- [10] A. Radke, T. Gissibl, T. Klotzbücher, P. V. Braun and H. Giessen, *Adv. Mater.* **2011**, 23, 3018–3021.
- [11] R. S. Rill, C. Plet, M. Thiel, I. Staude, G von. Freymann, S. Linden and M. Wegener, *Nat. Mater.* **2008**, 7, 543–546.
- [12] J. Walia, N. Dhindsa, M. Khorasaninejad and S. S. Saini, *Small* **2014**, 10, 144–151.

- [13] H. Masuda and K. Fukuda, *Science* **1995**, *268*, 1466–1468
- [14] P. Roy, S. Berger and P. Schmuki, *Angew. Chem., Int. Ed.* **2011**, *50*, 2904–2939.
- [15] J. Liu, J-Guang. Zhang, Z. Yang, J. P. Lemmon, C. Imhoff, G. L. Graff, L. Li, J. Hu, C. Wang, J. Xiao, G. Xia, V. V. Viswanathan, S. Baskaran, V. Sprenkle, X. Li, Y. Shao and B. Schwenzer, *Adv. Funct. Mater.* **2013**, *23*, 929-946.
- [16] Y. Tang, Z. Jiang, G. Xing, A. Li, P. D. Kanhere, Y. Zhang, T. C. Sum, S. Li, X. Chen, Z. Dong, and Z. Chen, *Adv. Funct. Mater* **2013**, *23*, 2932-2940
- [17] A. Tanaka, K. Hashimoto, H. Kominami, *J. Am. Chem. Soc.* **2013**, *136*, 586-589.
- [18] C. Hu, T. Peng, X. Hu, Y. Nie, X. Zhou, J. Qu, H. He. *J. Am. Chem. Soc.* **2010**, *132*, 857-862.
- [19] J. Yu, G. Dai, B. Huang. *J. Phys. Chem. C* **2009**, *113*, 16394-16401.
- [20] M. Jung, J. N. Hart, D. Boensch, J. Scott, Y. H. Ng, R. Amal, *Appl. Catal. A- Gen.* **2016**, *518*, 221-230.
- [21] W. Zhao, M. Zhang, Z. Ai, Y. Yang, H. Xi, Q. Shi, X. Xu, H. Shi, *J. Phys. Chem. C* **2014**, *118*, 23117-23125.
- [22] V-P. Gao, J. Liu, S. Lee, T. Zhang, D. D. Sun, *J. Mater. Chem.* **2012**, *22*, 2292-2298.
- [23] J. Zhang, Z. Yu, Z. Gao, H. Ge, S. Zhao, C. Chen, S. Chen, X. Tong, M. Wang, Z. Zheng, Y. Qin, *Angew. Chem. Int. Ed.* **2017**, *56*, 816-820.

- [24] B. A. Nail, J. M. Fields, J. Zhao, J. Wang, M. J. Greaney, R. L. Brutchey, F. E. Osterloh, *ACS Nano* **2015**, 9, 5135-5142.
- [25] J. Zhao, S. C. Nguyen, R. Ye, B. Ye, H. Weller, G. A. Somorjai, A. P. Alivisatos, F. D. Toste, *ACS Cent. Sci.* **2017**, 3, 482-488.
- [26] J. Sakamoto, T. Ohara, N. Yasumoto, Y. Shiraishi, S. Ichikawa, S. Tanaka, T. Hirai, *J. Am. Chem. Soc.* **2015**, 137, 9324-9332.
- [27] S. Sarina, H. Zhu, Q. Xiao, E. Jaatinen, J. Jia, Y. Huang, Z. Zheng, H. Wu, *Angew. Chem. Int. Ed.* **2014**, 53, 2935-2940.
- [28] G. Hao, B. K. Juluri, Y. B. Zheng, B. Wang, I-K. Chiang, L. Jensen, V. Crespi, P. C. Eklund, T. J. Huang, *J. Phys. Chem. C* **2010**, 114, 18059-18066.
- [29] M. L. Brongersma, N. J. Halas, and P. Nordlander, *Nat. Nanotechnol.* **2015**, 10, 25-34.
- [30] C. Clavero, *Nat. Photonics*, **2014**, 8, 95-103.
- [31] Y. Shiraishi, H. Sakamoto, Y. Sugano, S. Ichikawa and T. Hirai, *ACS Nano*, **2013**, 9287-9297.
- [32] Z. Ding, H. Yang, J. Liu, W. Dai, X. Chen, X. Wang, X. Fu, *Appl. Catal. B-Environ.* **2011**, 101, 326-332.
- [33] S. Xie, Y. Wang, Q. Zhang, W. Fan, W. Deng and Y. Wang, *Chem. Commun.* **2013**, 49, 2451-2453.
- [34] L. G. Devi, R. kavitha, *Appl. Catal. B: Environ.* **2013**, 140-141, 559-587.

- [35] K. Qian, B. C. Sweeny, A. C. Johnston-Peck, W. Niu, J. O. Grahan, J. S. DuChene, J. Qiu, Y-C. Wang, M. H. Engelhard, D. Su, E. A. Stach, and W. D. Wei, *J. Am. Chem. Soc.*, **2014**, 136, 9842-9845.
- [36] V. Subramanian, E. E. Wolf, and P. V. Kamat, *J. Am. Chem. Soc.*, **2004**, 126, 4943-4950.
- [37] G. L. Nealon, B. Donnio, R. Greget, J-P. Kappler, E. Terazzi and J-L. Gallani, *Nanoscale*, **2012**, 4, 5244-5258.
- [38] C. Mao, F. Zuo, Y. Hou, X. Bu and P. Feng, *Angew. Chem. Int. Ed.* **2014**, 53, 10485-10489.
- [39] H. J. Yun, D. M. Lee, S. Yu, J. Yoon, H-J. Park and J. Yi, *J. Mol. Catal. A: Chem.* **2013**, 378, 221-226.
- [40] Q. Liu, D. Ding, C. Ning, and X. Wang, *RSC Adv.*, **2015**, 5, 95478-95487..
- [41] C. K. Song, J. Baek, T. Y. Kim, S. Yu, J. W. Han, and J. Yi, *Appl. Catal. B-Envrion.*, **2016**, 198, 91-99.
- [42] S. Yu, S. Y. Lee, J. Yeo, J. W. Han, and J. Yi, *J. Phys. Chem. C* **2014**, 118, 29584-29590.
- [43] S. Yu, Y. H. Kim, S. Y. Lee, H. D. Song, and J. Yi, *Angew. Chem. Int. Ed.*, **2014**, 53, 11203-11207.
- [44] P. Vukusic, J. R. Sambles and C. R. Lawrence, *Nature*, **2001**, 409, 36-37.
- [45] S. Kinoshita, and S. Yoshioka, *ChemPhysChem*, **2005**, 6, 1442-1459.
- [46] H. Cong, and W. Cao, *Langmuir*, **2004**, 20, 8049-805.

- [47] B. Gralak, G. Taveb, and S. Enoch, *Optics Express*, **2001**, *9*, 567-578.
- [48] E. Yablonovich, *Phys. Rev. Lett*, **1987**, *58*, 2059-2062.
- [49] J. D. Joannopoulos, S. G. Johnson, J. N. Winn, and R. D. Meade, *Photonic Crystals: Molding the Flow of Light*, 2nd ed.; Princeton University Press: Princeton, New Jersey, **2008**; pp 32-35.
- [50] F. Vanmeert, G. V. D. Snickt, and K. Janssens, *Angew. Chem. Int. Ed.* **2015**, *54*, 3607–3610.
- [51] J. H. Braun, A. Baidins, and R. E. Marganski, *Organic Coatings*, **1992**, *20*, 105-138
- [52] Y. S. Do, J. H, Park, B. Y. Hwang, S-M. Lee, B-K. Ju and K. C. Choi, *Adv. Optical Mater.* **2013**, *1*, 133-138.
- [53] W. Zhang, M. Anaya, G. Lozano, M. E. Calvo, and M. B. Johnston, *Nano Lett*, **2015**, *15*, 1698-1702.
- [54] H. Kim, J. Ge, J. Kim, S. E. Choi, H. Lee, W. Park, Y. Yin, and Y. Kwon, *Nature Photonics*, **2009**, *3*, 534-540.
- [55] L. D. Bonifacio, B. V. Lotsch, D. P. Puzzo, F. Scotognella, and G. A. Ozin, *Adv. Mater.* **2009**, *21*, 1641–1646.
- [56] K. Seo, M. Wover, P. Steinvurzel, E. Schonburn, Y. Dan, T. Ellenboggen, and K. B. Grozier, *Nano Lett.* **2011**, *11*, 1851-1856.
- [57] J. Wali, N. Dhindsa, M. Khorasaninejad, S. S. Saini, *Small*, **2014**, *10*, 144-151.
- [58] S. J. Tan, L. Zhang, D. Zhu, X. M, Goh, Y. M. Wang, K. Kumar, C.-W. Oiu, J. K. Yang, *Nano Lett.* **2014**, *14*, 4023-4029.

- [59] Z.-Z. Gu, H. Uetsuka, K. Takahashi, R. Nakajima, H. Onishi, A. Fujishima, O. Sato, *Angew. Chem. Int. Ed.* **2003**, *42*, 894-897.
- [60] J. H. Moon and S. Yang, *Chem. Rev.* **2010**, *110*, 547-574.
- [61] M. Xiao, Y. Li, M. C. Allen, D. D. Deheyn, X. Yue, J. Zhao, N. C. Gianneschi, M. D. Shawkey, and A. Dhinojwala, *ACS Nano*, **2015**, *9*, 5454-5460.
- [62] J. H. Prosser, T. Brugarolas, S. Lee, A. J. Nolte, and D. Lee, *Nano Lett.* **2012**, *12* 5287-5291
- [63] J. Jin, K. Liu, and X. Chen *Small*, **2011**, *7*, 1784-1789.
- [64] B. Liu, K. Nakata, S. Liu, M. Sakai, T. Ochiai, T. Murakami, K. Takagi, and A. Fujishima, *J. Phys. Chem. C.* **2012**, *116*, 7471-7479.
- [65] F. G. Cheng, T.S. Luk, and X. Yang, *Sci. Rep.* **2015**, *5*, 1-10.
- [66] D. Choi, C. K. Shin, D. Yoon, D.S. Chung, Y. W. Jin, and L. P. Lee, *Nano Lett.* **2014**, *14*, 3374-3381.
- [67] J.-G. Park, S.-H. Kim, S. Magkiriadou, T. Choi, Y. Kim, and V. Manoharan, *Angew. Chem., Int. Ed.* **2014**, *53*, 2899–2903.
- [68] J. D. Forster, H. Noh, S. F. Liew, V. Saranathan, C. F. Schreck, L. Yang, J. Park, R. O. Prum, S. J. Mochrie, C. S. O'Hern, H. Cao, and E. R. Dufresne, *Adv. Mater.* **2010**, *22*, 2939–2944.
- [69] M. Kolle, P. M. Salgard-Cunha, M.R. Scherer, F. Huang, P. Vukusic, S. Mahajan, J. J. Baumberg, and U. Steiner, *Nat. Nanotechnol.* **2010**, *5*, 511–515.
- [70] S. Coyle, G. V. Prakash, J. J. Baumberg, M. Abdelsalem, and P. N. Bartlett, *Appl. Phys. Lett.* **2003**, *83*, 767-769.

- [71] K. Zhu, N. R. Neale, A. Miedaner, and A. J. Frank, *Nano Lett.* **2007**, 7, 69-74
- [72] E. R. Loewen and E. Popov, CRC Press, New York, USA, **1997**.
- [73] J.-T. Zhang, L. Wang, J. Luo, A. Tikhonov, N. Kornienko, and S. A. Asher, *J. Am. Chem. Soc.* **2011**, 133, 9152–9155.
- [74] X. Ye, Y. Li, J. Dong, J. Xiao, Y. Ma, and L. Qi, *J. Mater. Chem. C* **2013**, 1, 6112–6119.
- [75] K. Kumar, H. Duan, R. S. Hegde, S. W. Koh, J. N. Wei, and J. K. Yang, *Nat. Nanotechnol.*, **2012**, 7, 557-561
- [76] A. Kusnetzow, A. Dukkipati, K. R. Babu, D. Singh, B. W. Vought, B. E. Knox, and R. R. Birge, *Biochemistry* **2001**, 40, 7832–7844.
- [77] Y. Gu, L. Zhang, K. W. Yang, S. P. Yeo and C.-W. Qiu, *Nanoscale* **2015**, 7, 6409–6419.
- [78] Y. Zhao, Z. Xie, H. Gu, C. Zhu, and Z. Gu, *Chem. Soc. Rev.* **2012**, 41, 3297–3317.
- [79] S. Kment, F. Riboni, S. Pausova, L. Wang, L. Wang, H. Han, Z. Hubicka, J. Krysa, P. Schmuki and R. Zboril, *Chem. Soc. Rev.* **2017**, 46, 3716-3769.
- [80] N. T. Nguyen, M. Altomare, J. E. Yoo, N. Taccardi and P. Schmuki, *Adv. Energy. Mater.* **2016**, 6, 1501926.
- [81] Z. Zhang, L. Zhang, M. N. Hedhili, H. Zhang and P. Wang, *Nano let.* **2013**, 13, 14-20.

## 국 문 초 록

산업화 이후 화석연료의 사용량이 늘어나면서 환경 오염과 친환경 에너지 생산은 전 세계적으로 해결해야 할 문제로 대두되고 있다. 광촉매 기술은 태양광을 에너지원으로 하여 지속가능한 에너지 생산 방식 중 하나인 태양광 발전에 활용되고 있으며, 오염물 처리를 통한 환경정화에도 사용된다. 광촉매 물질로 가장 널리 다루어지고 있는 물질은 이산화티탄으로써, 넓은 범용성, 높은 안정성, 경제성 등 다양한 장점을 지니고 있다. 그러나 이러한 장점에도 불구하고 이산화티탄 기반 광촉매는 효율이 낮고, 이용할 수 있는 빛이 자외선 영역으로 제한된다는 단점을 지니고 있어 가시광 영역대의 빛을 활용하여 효율을 높이기 위한 방법이 필요하다. 이산화티탄의 밴드갭 에너지는 3.0 ~ 3.2 eV로 지구상으로 들어오는 태양광의 약 3 %만 존재하는 자외선 영역에 해당하기 때문에 고효율의 에너지를 얻기가 어렵다. 이를 해결하기 위해 본 연구에서는 나노 구조 제어 기술을 통해 물질의 전자 밴드 혹은 광 밴드를 조절함으로써 가시광 영역대의 빛을 활용할 수 있는 이산화티탄 광촉매를 제조하였다.

먼저 이산화티탄에 백금 나노입자를 담지하여 가시광 흡광율을 높이고 금속 나노입자의 페르미 준위를 조절하여 전하 분리에 미치는 영향을 확인하고자 하였다. 금속 나노입자의 페르미 준위가 이산화티탄과 백금 나노입자가 접합했을 경우 밴드 벤딩에 영향을 주는 것을 확인하였고

이는 전하 분리에도 영향을 미치는 것을 확인하였다. 가시광 하에서 백금 나노입자를 담지하지 않은 이산화티탄과 비교하였을 경우 기상 아세트알데히드의 높은 광분해율을 나타내었다.

표면 미세구조를 조절하여 색을 나타내는 구조색은 염료를 이용한 발색현상과 달리 무기소재의 미세구조 조절을 통해 색을 구현하였으므로 백화 현상이나 표백 현상이 일어나지 않으며, 화학적 처리에도 색을 유지하는 높은 안정성을 가질 수 있다. 본 연구에서는 미세구조와 빛의 상호작용을 통한 색 구현 메커니즘을 규명하고 제조가 간단한  $\text{TiO}_2$  나노보울구조를 이용하여 광결정 구조를 설계하였다. Bragg 식에 대한 이해를 통해 반영구적으로 색상이 유지되는 물질을 설계할 수 있었다. 이러한 설계 후 실험적 검증 방법은 향후 광결정 설계에 있어서 디자인 전략을 제시할 수 있으며, 이를 증명하기 위해 물분해를 통한 광전류 생산 실험을 진행하였다.

주요어: 이산화티탄, 불균일계 광촉매, 가시광 감응형, 페르미 준위, 전자 띠, 전하 분리, 아세트알데하이드기공성 구조, 구조색, 광결정, 광 띠, 물분해  
학 번: 2014-30292

## List of publications

### International Publications

#### International Academic Published Papers (First Author)

1. **H. N. Umh\***, S. Yu\*, Y. H. Kim, S. Y. Lee, and J. Yi (\*co-first author), “Tuning the Structural Color of a 2D Photonic Crystal using a Bowl-Like Nanostructure”, *ACS Applied Materials & Interfaces*, **8**(24), 15802-15808 (2016).
2. **H. N. Umh**, H. H. Shin, J. Yi and Y. Kim, “Fabrication of gold nanowires (GNW) using aluminum anodic oxide (AAO) as a metal-ion sensor”, *Korean Journal of Chemical Engineering*, **32**(2), 299-302 (2015).

#### International Academic Published Papers (Co-author)

1. S. Yu, S. Y. Lee, **H. N. Umh**, and J. Yi, “Energy conversion of sub-band-gap light using naked carbon nanodots and rhodamine B”, *Nano Energy*, **26**, 479-487 (2016)

### Patents

1. 이종협, 엄하늬, 유성주, 김용화, 이수영 “구조색을 지닌 이산화티탄 나노 기공성 필름 및 그 제조방법”, 대한민국특허 등록 10-1810328 (2017.12.12)

#### International Conferences (First author)

1. Poster presentation, **H. N. Umh**, S. Yu, Y. H. Kim, S. Y. Lee, H. D. Song, and J. Yi, “Realization of Inorganic Structural Colors of a 2D Photonic Crystal.”, 2016 MRS Fall Meeting Program & Exhibit, Boston, Massachusetts, USA, Nov. 27-Dec. 2, 2016

### International Conferences (Co-author)

1. Poster presentation, S. Y. Lee, S. Yu, **H. N. Umh**, S. Shin, S. E. Jerng, and J. Yi, “FRET-Assisted Upconversion of Organic Quantum Dots for the Utilization of Below-Bandgap Solar Energy.”, 2016 MRS Fall Meeting Program & Exhibit, Boston, Massachusetts, USA, Nov. 27-Dec. 2, 2016
2. Poster presentation, S. Yu, S. Y. Lee, Y. H. Kim, **H. N. Umh**, and J. Yi, “Z-Schematic Electron-Transfer Kinetics of the All-Solid-State Photocatalyst Working at Visible Light.”, 27th International Conference on Photochemistry, ICC Jeju, Jeju Island, Korea, June. 28-July. 3, 2015
3. Poster presentation, S. Yu, S. Y. Lee, Y. H. Kim, **H. N. Umh**, J. Park, and J. Yi, “Reaction Routes and Electron Transfer at Hetero-Interfaces of Catalysts for Artificial Photosynthesis”, The 15<sup>th</sup> Korea-Japan Symposium on Catalysis, BEXCO and Haeundae Centum Hotel, Busan, Korea, May. 26-28, 2015
4. Poster presentation, S. Yu, Y. H. Kim, S. Y. Lee, H. D. Song, **H. N. Umh**, and J. Yi, “Plasmon-enhanced solar energy conversion to chemical and electrical energy”, 248<sup>th</sup> American Chemical Society National Meeting & Exposition, San Francisco, CA, USA, Aug. 10-14, 2014
5. Poster presentation, I. Nam, G.-P. Kim, S. Park, J. W. Han, S. Bae, S. Yu, **H. N. Umh**, S. Y. Lee, Y. H. Kim, and J. Yi, “High voltage energy storage systems using facile patterning approach”, 248<sup>th</sup> American Chemical Society National Meeting & Exposition, San Francisco, CA, USA, Aug. 10-14, 2014

- Poster presentation, J. Baek, T. Y. Kim, I. Nam, S. Park, S. Yu, S. Bae, S. Y. Lee, **H. N. Umh**, Y. H. Kim, and J. Yi, “Production of valuable chemicals (1,3-butadiene) from biomass-based resources alternative to the petroleum”, , 248<sup>th</sup> American Chemical Society National Meeting & Exposition, San Francisco, CA, USA, Aug. 10-14, 2014

## Domestic Conferences

- 김용화, 정성은, 유영근, 박종석, **엽하늬**, 배성준, 이수영, 김영훈, 최진희, 이종협, “Environmental Impact Analysis of Perovskite and Silicon Solar Cell via Life-cycle Assessment” 페로브스카이트 포토닉스 학술대회, 2017년도, 라마다프라자제주호텔, 11. 20-21 (2017)
- 이수영, **엽하늬**, 배성준, 유영근, 박종석, 김용화, 정성은, 김영훈, 최진희, 이종협, “Environmental Safety Assessment of Perovskite Solar Cell”, 페로브스카이트 포토닉스 학술대회, 2017년도, 라마다프라자제주호텔, 11. 20-21 (2017)
- 배성준, 유영근, 박종석, 송현돈, **엽하늬**, 이수영, 김용화, 정성은, 이종협, 한정우, “지르코니아 표면 특성으로 인한 리튬산소전지의 방전생성물 안정화 연구”, 한국화학공학회 2017년도 봄 총회 및 학술대회, 제주 ICC, 4. 26-28 (2017)
- 이수영, 유성주, **엽하늬**, 송현돈, 신수지, 이종협, “유무기 접합 시스템을 통한 밴드갭 이하의 광에너지 전환”, 한국화학공학회 2016년도 봄 총회 및 학술대회, 부산 BEXCO, 4. 27-29 (2016)
- 엽하늬**, 유성주, 김용화, 이수영, 송현돈, 김혜선, 신수지, 이종협, “나비 날개를 모사한 이산화티탄 나노튜브 표면의 구조색 제어”, 한국화학공학회 2016년도 봄 총회 및 학술대회, 부산 BEXCO, 4. 27-29 (2016)
- 유성주, 이수영, 김용화, **엽하늬**, 이종협, “물로부터 청정연료 수소생산을 위한 광촉매의 반응기작”, 2015년 한국청정기술학회 춘계 학술발표회, 부여 롯데리조트, 3. 26-27 (2015)
- 유성주, 김용화, 이수영, **엽하늬**, 이종협, “물로부터 수소와 전기 생산을

위한 청정기술 개발”, 2015년 한국청정기술학회 춘계 학술발표회, 부여  
롯데리조트, 3. 26-27 (2015)